INL/RPT-23-75506
Revision 0

Scaling Outlooks on Integrated Energy Systems

October | 2023

Ramon Yoshiura, Sarah Creasman, Nipun Popli, and Aaron Epiney
Idaho National Laboratory

IES
Integrated Energy Systems

INL/RPT-23-75506
Revision 0

Scaling Outlooks on Integrated Energy Systems

Ramon Yoshiura, Sarah Creasman, Nipun Popli, and Aaron Epiney
Idaho National Laboratory

October | 2023

Idaho National Laboratory
Integrated Energy Systems
Idaho Falls, Idaho 83415

http://www.ies.inl.gov

Prepared for the
U.S. Department of Energy
Office of Nuclear Energy
Under DOE Idaho Operations Office
Contract DE-AC07-05ID14517

Page intentionally left blank

SUMMARY

This report provides research summaries of two developed theories: (1) data projection to enable multiscale facility digital interactions; and (2) introducing the Evaluation Model Development and Assessment Process (EMDAP) approach to integrated energy systems (IES) design. For data projection, a two-system scaling case including interactions between thermal storage and hydrogen production is provided. The corresponding facilities are the thermal energy distribution system (TEDS) facility and the high-temperature steam electrolysis (HTSE) facility at the Dynamic Energy Transport and Integration Laboratory (DETAIL) at Idaho National Laboratory (INL). For the EMDAP adaption to system design, a modified EMDAP process was developed and applied to an indirect two-tank heat storage system design. System phenomena were identified, ranked, and scaled to discover helpful key relations that would determine the ideal component geometry.

Page intentionally left blank

CONTENTS

FIGURES

TABLES

Page intentionally left blank

ACRONYMS

ANPP	advanced nuclear power plant
BOP	balance of plant
CHX	charging heat exchanger
DC	direct current
DETAIL	Dynamic Energy Transport and Integration Laboratory
DHX	discharging heat exchanger
DSS	dynamical system scaling
Dymola	Dynamic Modeling Laboratory
EMDAP	Evaluation Model Development and Assessment Process
FOM	figures of merit
HTSE	high-temperature steam electrolysis
HX	heat exchanger
IES	integrated energy systems
IET	integral effects test
IHX	intermediate heat exchanger
INL	Idaho National Laboratory
NPP	nuclear power plant
NRC	U.S. Nuclear Regulatory Commission
NTU	number of transfer units
PID	proportional-integral-derivative
PIRT	phenomena identification and ranking table
SET	separate effects test
SG	steam generator
SOEC	solid-oxide electrolysis cell
TEDS	thermal energy distribution system
TES	thermal energy storage
TTSS	thermocline thermal storage system
U.S.	United States

Page intentionally left blank

Scaling Outlooks on Integrated Energy Systems

1. INTRODUCTION

As the energy infrastructure diversifies, and in light of new worldwide zero-carbon initiatives, integrated energy systems (IES) are a flexible solution to optimally dispatch energy [1]. To make a waste-free and adaptable energy infrastructure a reality, innovative energy production strategies and method of distribution are essential. This includes considering the local and global effects of coupled electric and thermal energy source utilities and their associated users. Recent examples of optimal control failure leading to catastrophic outcomes include Texas in 2021 where record-breaking low temperatures impaired electricity utilities while increasing power demand [2], and Argentina in 2022 when unprecedented high temperatures partially disabled power production and triggered higher electricity demand to such an extent as to limit the water-purification system, thereby affecting the supply [3]. As fossil-fuel power utilities—those without the capability for carbon capture (e.g., direct-air capture systems [4]) to be at least carbon neutral—are decommissioned or replaced, and industrial processes convert to non-carbon-emitting sources for heat or other energy forms (such as steam), macro- and micro-grids must adapt to the load-balance daily demand. Another crucial component of future conversions towards zero carbon is an assessment of commodities and product prices due to different process shifts, which can be assessed via techno-economic analyses. For this reason, it is increasingly important to build IES capabilities to account for variants, such as daily demand and seasonal changes, to successfully load-balance and maximize profits for hour-ahead, day-ahead, or real-time markets [5].

Looking forward to realizing a functioning IES is a coupled equation of understanding system requirements and demonstrating the developed capabilities at a reduced-scale to ensure the feasibility, reliability, and effectiveness. As multiple entities such as nuclear power plants (NPPs), solar power units, hydrogen production facilities, and other possible processes are integrated, each system will require certain operating conditions that will limit system to system compatibility. As an example, coupling for NPPs to accommodate pulp and paper manufacturing units, a system that typically exhibits diurnal variations in its thermal load profile, will require long-term duration heat storage. However, identifying a suitable heat storage technology that will satisfy both sides is a non-trivial task; demonstrating that capability can be expensive. Using scaling methodologies to enable digital multiscale facility real-time interactions or design pilot-scale demonstrations are possible solutions that can remove the uncertainty in technology applicability and provide insights on new operational conditions and geometric designs that conserve the governing laws and physics.

To provide a summary of the conducted research using scaling methodologies to fill the gap in realizing IES, this report includes two research topics: (1) data projection; and (2) scaling-aided system design. For data projections, a two-system scaling case including interactions between thermal storage and hydrogen production is provided. The corresponding facilities are the thermal energy distribution system (TEDS) facility and the high-temperature steam electrolysis (HTSE) facility at the Dynamic Energy Transport and Integration Laboratory (DETAIL) at Idaho National Laboratory (INL). The scaling analysis considered both top and bottom scaling to conserve the properties of each system. The selected demonstration tool was the Dynamic Modeling Laboratory (Dymola), a commercially available Modelica-based modeling and simulation environment for engineering applications [6,7]. For the scaling-aided system design, a nuclear power industry standard was applied to strengthen the design process. As a simple application case, the developed design process was applied to an indirect two-tank heat storage system. The structure of this report follows three major sections: (1) dynamical system scaling (DSS) theory; (2) data projection; and (3) scaling informed design.

2. DYNAMICAL SYSTEM SCALING

Before introducing the specific cases that will describe the data projections and scaling informed design in Sections 3 and 4, the high-level explanation of DSS theory will be provided as a source to understand how mathematically all postprocessing variables are connected. A more complete derivation and DSS approach to system scaling is based on transforming the typical view of a process into a special coordinate system in terms of the parameter of interest and its agents of change [8]. By parameterizing a process using a time term, which is introduced later in this section, the reproduced data can be converted into the special three-coordinate system (also called the phase space) and form a geometry with curves along the surface that contain invariant and intrinsic properties. The remainder of this section is a review of DSS theory, which was introduced by Reyes [8,9,10]. The parameter of interest is defined as a conserved quantity within a control volume:

$$\beta(t) = \frac{1}{\Psi_0} \iiint_V \psi(\vec{x}, t)\, dV \tag{1}$$

where

β = is defined as the volume integral of the time- and space-dependent conserved quantity

ψ = when normalized by a time-independent value

Ψ_O = characterizes the process.

The agents of change are defined as the first derivative of the normalized parameter of interest. The changes are categorized into volumetric, surface, and quantity transport components:

$$\omega = \frac{1}{\Psi_0}\frac{d}{dt} \iiint_V \psi(\vec{x}, t)\, dV = \iiint_V \left(\phi_v + \phi_f\right) dV + \iint_A (\vec{j} \cdot \vec{n})\, dA - \iint_A \psi(\vec{v} - \vec{v}_s) \cdot \vec{n}\, dA \tag{2}$$

where

$\vec{x}$ = a position

t = measurement of time

$\vec{v}$ = medium velocity

$\vec{v}_x$ = local instantaneous surface velocity

$\vec{n}$ = outward normal vector

$\vec{j}$ = surface flux.

Combined, the local and instantaneous amount of a conserved quantity, $\psi(\vec{x}, t)$, is about the quantity that can change by material transportation, $\psi(\vec{v} - \vec{v}_s) \cdot \vec{n}$, into or out of the control volume, surface change applied to the surface, $(\vec{j} \cdot \vec{n})$, volumetric sources or sinks, ϕ_v, and action of external fields, ϕ_f. The agents of change are also the sum of the individual agents of change:

$$\omega(t) = \frac{1}{\Psi_0}\frac{d}{dt} \iiint_V \psi(\vec{x}, t) = \sum_{i=1}^{n} \omega_i \tag{3}$$

The relationship between ω and β is the following:

$$\omega(t) = \left.\frac{d\beta}{dt}\right|_t = \sum_{i=1}^{n} \omega_i \tag{4}$$

where ω is the first derivative of the reference time. Reference time is, as defined in Einstein and Infeld, a value that moves in constant increments independent of any process [11]. For a given process, considering each data point in a given transient exists, the reference time and amount of conserved quantity within the control volume can be identified as a state of the system. However, this concept lacks information regarding the direction in which a process is evolving. To address the direction of the

process, a parametric time dependent on the changes is required instead of reference time. The process-dependent timescale introduced in DSS is called the process time:

$$\tau(t) = \frac{\beta(t)}{\omega(t)} \tag{5}$$

Using the defined parameter of interest, (β), agents of change, (ω), and process time, (τ), a new state-space geometry can be defined by the β-ω-τ coordinate phase space. The word *geometry* in this context refers to the space generated by the possible processes a system can experience. Thus, a process is merely a curve along the system data geometry surface. Setting the axes along the system data geometry surface as β and ω, the distance between two points on the surface (or two states in a given transient) can be described as the amount change between one state to another, as shown in Figure 1.

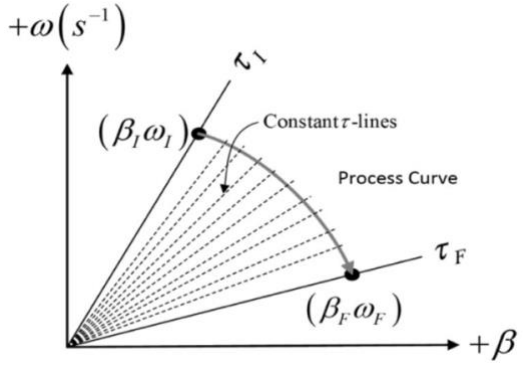

Figure 1. The β-ω-τ coordinate system with the representation of data evolution defined with changing process time where subscript "*I*" is the initial state and "*F*" is the final state [10]. The "s^{-1}" is an example of frequency. In this case, it would be per second.

To measure the progression difference between the reference time and process time in terms of the reference time, the idea of temporal displacement rate (D) is adopted:

$$D(t) = \frac{d\tau - dt}{dt} = -\frac{\beta}{\omega^2}\frac{d\omega}{dt} \tag{6}$$

From Equation (6), a finite and infinitesimal process and reference time interval expression reveals how the temporal displacement rate affects the time dependent relation. For $D > 0$, the process time interval is dilated in comparison to the reference time interval. For $D = 0$, both time intervals are equivalent describing the state change measured by process time as a natural parameterization is, as measured in reference time. For $D < 0$, the process time interval is contracted in comparison to the reference time interval. To measure the distance traveled from one state to another, the interval of the process time is determined, and is called the process action:

$$d\tau = \tau_S = \int (1 + D)\, dt \tag{7}$$

Here, an additional layer of normalization is provided to enhance the representation of the given process. This is done by normalizing via the process action (τ_S) for postprocessed variables with remaining time units. The normalization is conducted by canceling existing units in the agents of change, (ω), process time, (τ), and reference time, (t). Applying the process action to normalize the phase space coordinates produces the following normalized terms:

$$\widetilde{\Omega} = \omega\tau_S,\ \tilde{t} = \frac{t}{\tau_S},\ \tilde{\tau} = \frac{\tau}{\tau_S} \tag{8}$$

The normalized agents of change is also referred to as the effect parameter, and is used with the parameter of interest to visualize the phase space of the transient. A representation of the phase space diagram is provided in Figure 2. Using the stated coordinate system and transforming to the

time-normalized phase space of β-$\widetilde{\Omega}$-$\tilde{\tau}$, the scaling relationship between the prototype and model (a transformed system) can be defined for both β and ω and represents the scaling of the parameter of interest and its corresponding agents of change (or the frequency obtained from the units of time). The scaling relationship for the parameter of interest is λ_A, while for the agents of change is λ_B:

$$\lambda_A = \frac{\beta_M}{\beta_P},\ \lambda_B = \frac{\omega_M}{\omega_P} \tag{9}$$

where the subscripts M and P stand for the model and prototype, respectively. For λ_A, similar to the temporal displacement rate, different scaling effects are exhibited in respect to the default value of 1. Following the format shown in Equation (1) for $\lambda_A > 1$, the relative parameter of interest raw value would be Ψ if the model system is larger than the prototype system. For $\lambda_A = 1$, the relative raw value is the same. Note this does not imply that the values are equivalent. Rather, compared to the parameter of interest nominal value of the given process, the values remain the same. For $\lambda_A < 1$, the relative raw value of the model system is smaller than the prototype system. Although the default value for λ_B is 1, implications of the scaling ratio values are different in comparison to λ_B. For $\lambda_B > 1$, the first-order change and the associated reference time series are slower than the prototype system. For $\lambda_B = 1$, the first-order effects are equivalent to the prototype system. For $\lambda_B > 1$, the first-order effects are faster than the prototype system. The application of λ_A and λ_B to Equations (5), (6), and (8) provides the scaling ratios for other parameters as well:

$$\frac{t_M}{t_P} = \frac{\lambda_A}{\lambda_B},\ \frac{\tau_M}{\tau_P} = \frac{\tau_{S,M}}{\tau_{S,P}} = \frac{\lambda_A}{\lambda_B},\ \frac{\widetilde{\Omega}_M}{\widetilde{\Omega}_P} = \lambda_A,\ \frac{\tilde{\tau}_M}{\tilde{\tau}_P} = 1,\ \frac{D_M}{D_P} = 1 \tag{10}$$

The normalized agent of change is the sum, which is the same in reference to Equation (4):

$$\widetilde{\Omega} = \sum_{i=1}^{k} \widetilde{\Omega}_i \tag{11}$$

The ratio of $\widetilde{\Omega}$ is expressed in the following alternative form:

$$\widetilde{\Omega} = \frac{\widetilde{\Omega}_M}{\widetilde{\Omega}_P} = \frac{\sum_{i=1}^{k} \widetilde{\Omega}_{M,i}}{\sum_{i=1}^{k} \widetilde{\Omega}_{P,i}} = \frac{\widetilde{\Omega}_{M,1}+\widetilde{\Omega}_{M,2}+\cdots+\widetilde{\Omega}_{M,k}}{\widetilde{\Omega}_{P,1}+\widetilde{\Omega}_{P,2}+\cdots+\widetilde{\Omega}_{P,k}} \tag{12}$$

In reality, the agent of change scaling ratio, $\lambda_{A,i} = \frac{\widetilde{\Omega}_{M,i}}{\widetilde{\Omega}_{P,i}}$ (not agents of change, which is the sum), can be any value as long as the set agents of change scaling ratio, λ_A, is maintained. The strictest condition to apply is enforcing $\lambda_{A,i}$ to be equivalent to λ_A everywhere:

$$\lambda_A = \frac{\widetilde{\Omega}_{M,1}}{\widetilde{\Omega}_{P,1}} = \lambda_{A,1} = \frac{\widetilde{\Omega}_{M,2}}{\widetilde{\Omega}_{P,2}} = \cdots \lambda_{A,k} = \frac{\widetilde{\Omega}_{M,k}}{\Omega_{P,k}} \tag{13}$$

This follows the law of scaled ratios as each agent of change postulated in Equation (2) will be regulated to have the equivalent scaling ratio of ω. From Reyes, the scaling methods and similarity criteria are subdivided into five categories: (1) 2–2 affine; (2) dilation; (3) β-strain; (4) ω-strain; and (5) identity [8]. Table 1 summarizes the similarity criteria. Despite the five categories, in essence, all are 2–2 affine, with the exception of the partial scaling ratio values being 1.

Table 1. Scaling methods and similarity criteria that result from two-parameter transformations [8].

Basis for Process Space-Time Coordinate Scaling				
Metric Invariance	$d\tilde{\tau}_P = d\tilde{\tau}_M$	and	Covariance Principle	$\frac{1}{\omega_P}\frac{d\beta_P}{dt_P} = \frac{1}{\omega_M}\frac{d\beta_M}{dt_M}$
$\beta - \omega$ Coordinate Transformations				
2-2 Affine	Dilation	β-Strain	ω-Strain	Identity
$\beta_R = \lambda_A$	$\beta_R = \lambda$	$\beta_R = \lambda_A$	$\beta_R = 1$	$\beta_R = 1$
$\omega_R = \lambda_B$	$\omega_R = \lambda$	$\omega_R = 1$	$\omega_R = \lambda_B$	$\omega_R = 1$
Similarity Criteria				
$\widetilde{\Omega}_R = \lambda_A$	$\widetilde{\Omega}_R = \lambda$	$\widetilde{\Omega}_R = \lambda_A$	$\widetilde{\Omega}_R = 1$	$\widetilde{\Omega}_R = 1$
$\tau_R = t_R = \frac{\lambda_A}{\lambda_B}$	$\tau_R = t_R = 1$	$\tau_R = t_R = \lambda_A$	$\tau_R = t_R = \frac{1}{\lambda_B}$	$\tau_R = t_R = 1$

The selection process is completely dependent on the system to be scaled and the restrictions applied. According to personal experience, limitations such as geometry, material properties, and manufacturing methods are major components that constrain the available types capable of scaling while abiding by research objectives.

To measure the similarity or difference between two processes, the local separation for each corresponding data point to measure is along the constant normalized process time indicating a comparison between two identical states [8]. This distance (η) is calculated using Equation (14) and is shown in Figure 2 where the straight line represents the curve of constant normalized process time. Although in Figure 2 the constant normalized process time is a straight line and using the Pythagorean theorem to calculate the distance may appear valid, this is only valid for flat surfaces and is helpful for visual data evaluation.

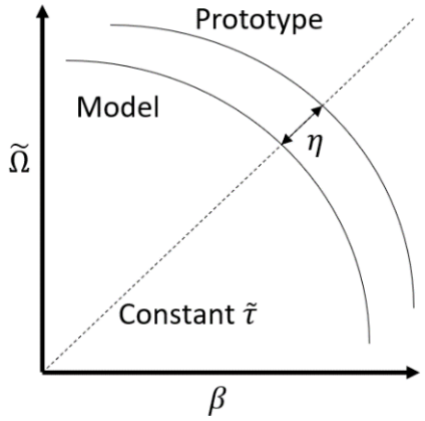

Figure 2. Phase space defined by the effect parameter ($\tilde{\Omega}$) and parameter of interest (β). η is the geodesic distance between the model and prototype data points along a constant normalized process time.

For any process curve, the distance measured for any Riemannian geometry is the following:

$$\tilde{\eta}(t) = \beta_P(t_P)\sqrt{\varepsilon D_P(t_P)}\left[\frac{1}{\widetilde{\Omega}_P(t_P)} - \frac{1}{\widetilde{\Omega}_M(t_M)}\right] \quad (14)$$

The sum of each temporal separation is the total distortion. To evaluate the overall separation, the standard error based on each local separation is the following:

$$\sigma_{est} = \sqrt{\frac{1}{N}\sum_{k=1}^{N}\tilde{\eta}^2(t)} \tag{15}$$

The calculated standard error is the band along the constant normalized process time curves and is perpendicular in direction. Effectively, by setting the number of standard errors, the confidence intervals falling within plus and minus the number of standard errors can be determined.

3. DATA PROJECTION

To solve the concern of interacting entities of different scales, regardless of whether it is possible to digitally communicate in real-time, a system to system adapter for incoming and outgoing signals preserving either system based on DSS data postprocessing was proposed. The basic function was to convert values to different scales (e.g., down-scale, up-scale, accelerate, decelerate) and reorganize the time series at the timescale of the intercepting system. To demonstrate this capability, the accelerated case of a heat storage and hydrogen production IES was selected with the following tasks:

- Establish the framework to understand the requirements of how scaling ratios in one system will affect other connecting systems
- Prepare and scale a demonstration case
- Validate the scaling analysis via system code.

3.1 Application Case

In order to accomplish these particular efforts, a two-system scaling case, including interaction between the TEDS and HTSE facilities, was selected. The scaling analysis considered both top and bottom scaling to conserve the properties of each system. The selected demonstration tool, Dymola, is a commercially available Modelica-based modeling and simulation environment for engineering applications [6,7]. The Dymola tool uses the Modelica modeling language [12], which has a causal connection of components governed by mathematical equations to facilitate modeling from first principles. Since modern scaling methodologies rely on and are based on first principles to determine the scaling relationships between the parameters of interest, compatibility with the Modelica language is high and identifies Dymola as the primary candidate to conduct the scaling validation. Specific models for TEDS and HTSE were developed prior to this research. Ideally, both models would be under the same simulation to demonstrate the two-system scaling effects. After the scaled equations for both systems were derived and test case simulations were available, the accelerated scaling ratios were determined, and the projected data was calculated. After the scaled initial and boundary conditions were implemented, the accelerated Dymola model data set was generated. By comparing the accelerated simulation data and the projected, scale-based data, the scaling efforts were evaluated. The scaling distortions were larger than anticipated and triggered a series of reinvestigations to improve the implemented scaling analysis. Adjustments of the scaling analysis were successful and indicated the validity of utilizing dynamic scaling methods to anticipate changes in operating conditions, required configuration changes, and appropriate sizing of components based on the first principles and a similarity assessment from the applied research. Although this method cannot replace design or experimental engineering, the information derived from the proposed research brings invaluable insights and justification to future IES architecture. The following sections supplement details of the data projection study. For further details beyond this report, review Reference [13].

3.2 Scaled System Equations

In the study, the components consisting of a combined heat storage and hydrogen production IES were considered. Although in a large-scale setup an IES could potentially utilize different technologies or equipment, the experimental setup existing in TEDS and HTSE were set as the target systems to apply the scaling methodologies. For TEDS, two heat exchangers (HXs), intermediate piping, and a thermocline tank were identified as the major subsystems to investigate. The TEDS facility is a thermal storage system at DETAIL, which specializes in thermal storage and discharge. The heat transfer and storage fluid is Therminol-66, a high-performance, highly stable synthetic heat transfer fluid. It is circulated around the loop acting as the main media providing thermal stability without forming volatile or highly viscous products between operating temperatures of -85°C and 400°C. To increase the thermal storage capacity, an alumina filler is added to the thermocline [1]. The two HXs represent the heat source and sink of the heat storage system where the discharged energy is effectively a steam generator (SG) in the proposed IES as it is required for the electrolysis process in the HTSE cell stacks.

For HTSE, one SG, steam preheater, and furnace stack tank were identified as the major subsystems to investigate. The HTSE is another facility situated in the vicinity of DETAIL to demonstrate steam electrolysis at different stack powers. The stack is a solid-oxide electrolysis cell (SOEC) capable not only of running in electrolysis cell mode to generate steady amounts of hydrogen, but also designed to run in fuel-cell mode, creating electricity. Compared to the proton-exchange membrane and high-temperature thermochemical processes, SOECs are net zero carbon (if carbon dioxide is added to the cathode inlet, electrolysis of carbon dioxide is possible, thus making SOEC net-negative carbon) and are highly efficient due to minimal applied stack voltage. The hydrogen recycler process retrieves 10% of the produced hydrogen to prevent the oxidation of furnace stack components and is initiated when the SOEC is ongoing.

Altogether, the scaled results of all acknowledged processes of subsystems are provided in Table 2. In order to ensure how one objective scaling ratio affects other connected subsystem process scaling ratios, the chain of processes was considered. In total, nine chains were identified: (1) source HX tube outlet temperature and intermediate piping inlet temperature ($\lambda_{A,T_{tube,out}} = \lambda_{A,T}$); (2) intermediate piping outlet velocity and thermocline inlet velocity ($\lambda_{A,v_z} = \lambda_{A,v_{z,in}}$); (3) thermocline outlet velocity and intermediate piping inlet velocity ($\lambda_{A,v_{z,out}} = \lambda_{A,v_z}$); (4) intermediate piping outlet temperature and SG tube-side inlet temperature ($\lambda_{A,T} = \lambda_{A,T_{tube,in}}$); (5) SG shell-side outlet temperature and intermediate piping inlet temperature ($\lambda_{A,T_{shell,out}} = \lambda_{A,T}$); (6) intermediate piping outlet temperature and preheater inlet temperature ($\lambda_{A,T} = \lambda_{A,T_{in}}$); (7) preheater outlet temperature and stack inlet temperature; (8) stack outlet temperature and intermediate piping inlet temperature ($\lambda_{A,T_{out}} = \lambda_{A,T}$); and (9) intermediate piping outlet temperature and SG shell-side inlet temperature ($\lambda_{A,T} = \lambda_{A,T_{shell,in}}$). To locate the TEDS side connections, Figure 3 shows the locations of the TEDS side connections, while Figure 5 shows the locations of the HTSE-side connections.

Table 2. Scaled subsystem processes for the TEDS and HTSE facilities. Nomenclature can be found in [13].

Facility	Subsystem	Governing Equation Type	Scaled Equation
TEDS	HX (includes SG)	Overall Heat Transfer	$\left[\frac{1}{h_0}\right]\lambda_{A,Q} = \left[\frac{A_o}{A_i}\left(\frac{OD-ID}{k_w}\right)\right]_R = \left[\frac{A_o}{A_i}\left(\frac{1}{h_i}\right)\right]_R =$ $\left[\frac{\dot{m}LN_P F_T OD}{\rho v_{T.0} Q_0 ID^2}\right]_R \left[\frac{1}{\ln\left(\frac{T_{shell,in}-T_{tube,in}}{T_{shell,out}-T_{tube,out}}\right)}\right]_R \left[T_{tube,out,0}\right]_R \frac{\lambda_{A,T_{tube,out}}}{\lambda_{A,v_T}}$
	Intermediate Piping	Overall Heat Transfer	$\lambda_{B,\rho} = \left[\frac{v_{z,0}}{\Delta z}\right]_R \lambda_{A,v_z}\lambda_{A,\rho}, \quad t_R = \frac{\Delta z_R}{\lambda_A, v_z}$ $\lambda_{B,v_z} = \left[\frac{\nu}{r^2}\right]_R, \quad \lambda_{B,T} = \left[\frac{\mu}{\rho_0 T_0 c_P r}\right]_R \frac{\lambda_{A,v_z}}{\lambda_\rho}$
	Thermocline Tank	Fluid Mass Conservation Mixed Momentum Conservation Fluid Energy Conservation	$\lambda_{B,th} = \left[\frac{\rho_{in} R_{in} v_{z,in,0} c_{P,in}}{\rho_{th} c_{P,th} R_{th}^2 \Delta z}\right]_R \lambda_{A,v_{z,in}}\lambda_{A,th}, \lambda_{B,th} = \left[\frac{kT_{w,0}}{\rho_{th}\varepsilon R_{th}^2 T_{th,0}}\right]_R \frac{\lambda_{A,T_w}}{\lambda_{A,r}}$
HTSE	Steam Preheater	Preheater Thermal Dynamics	$\lambda_{B,th} = \left[\frac{\rho_{in} R_{in} v_{z,in,0} c_{P,in}}{\rho_{th} c_{P,th} R_{th}^2 \Delta z}\right]_R \lambda_{A,v_{z,in}}\lambda_{A,th}, \lambda_{B,th} = \left[\frac{kT_{w,0}}{\rho_{th}\varepsilon R_{th}^2 T_{th,0}}\right]_R \frac{\lambda_{A,T_w}}{\lambda_{A,r}}$
	Furnace Stack	Stack Electrical Dynamics • Reversible Overvoltage • Ohmic Overvoltage • Activation Overvoltage Stack Thermal Dynamics	$\lambda_{B,th} = \left[\frac{\rho_{in} R_{in} v_{z,in,0} c_{P,in}}{\rho_{th} c_{P,th} R_{th}^2 \Delta z}\right]_R \lambda_{A,v_{z,in}}\lambda_{A,th}, \lambda_{B,th} = \left[\frac{kT_{w,0}}{\rho_{th}\varepsilon R_{th}^2 T_{th,0}}\right]_R \frac{\lambda_{A,T_w}}{\lambda_{A,r}}$ $\lambda_{B,\bar{T}} = \left[\frac{n_c I \Delta H_0}{\bar{T}_0 C_{P,SOEC}}\right]_R \lambda_{A,\Delta H} = \left[\frac{P_{heat}}{\bar{T}_0 C_{P,SOEC}}\right]_R \lambda_{A,P_{heat}}$ $= \left[\frac{c_{P,H_2} n_c I \pi_{ca} P_{H_2,in} T_{out,0}}{\bar{T}_0 C_{P,SOEC} P_{H_2 0,in}}\right]_R \lambda_{A,T_{out}}$

3.3 Dymola Test Case and Models

For validation of the TEDS and HTSE scaling efforts, simulation or experimental data are required. But because maintenance is ongoing currently at TEDS and HTSE, Dymola was used for the modeling and simulation of integrated and complex systems to generate the needed data. The TEDS and HTSE Modelica models were developed from previous INL IES efforts and can be found in References [13,15]. The simulation results shown in Section 3.5 are the generated simulation data. These results are postprocessed to determine the initial and boundary conditions and data of the projected cases using the derived scaling equations from Table 2.

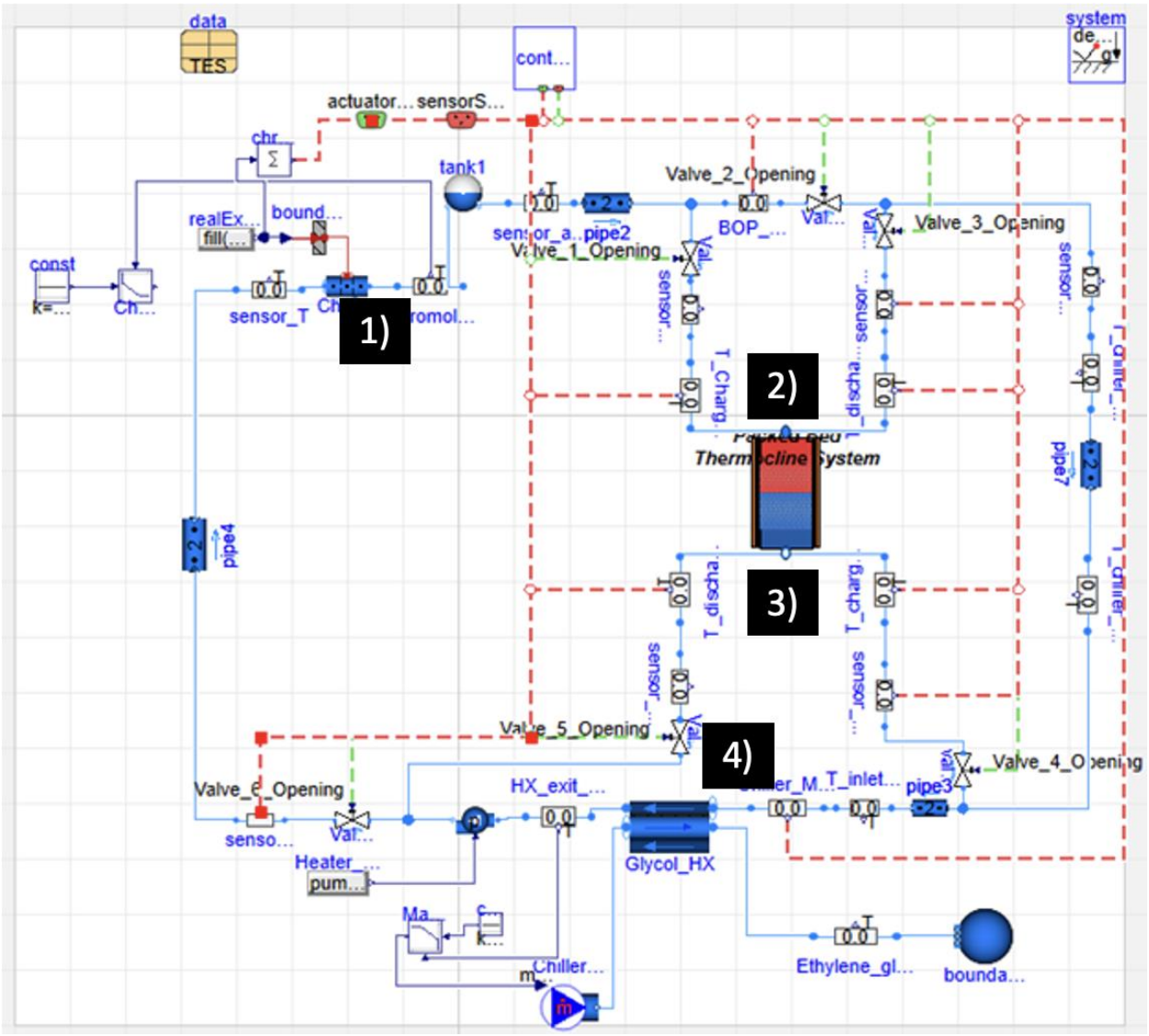

Figure 3. Overview of TEDS schematic and connection series location.

A single-tank packed-bed thermocline tank is used in TEDS for energy storage. A thermocline system uses hot and cold fluid, which are separated by a thin thermocline region, to store heat. The position of the thermocline moves depending on whether charging or discharging occurs. Hot fluid is pumped into the top of the tank, while cold fluid exits at the bottom of the tank during the charging mode. During discharge, cold fluid enters the bottom of the tank, while hot fluid exits from the top of the tank. The thermocline system is split into 200 axial nodes, each of which incorporates both a solid and fluid component. The inlets to and outlets from the thermocline can be seen in Figure 4, as well as sensors for the mass flow rate and temperature of the inlet and outlet during both charging and discharging.

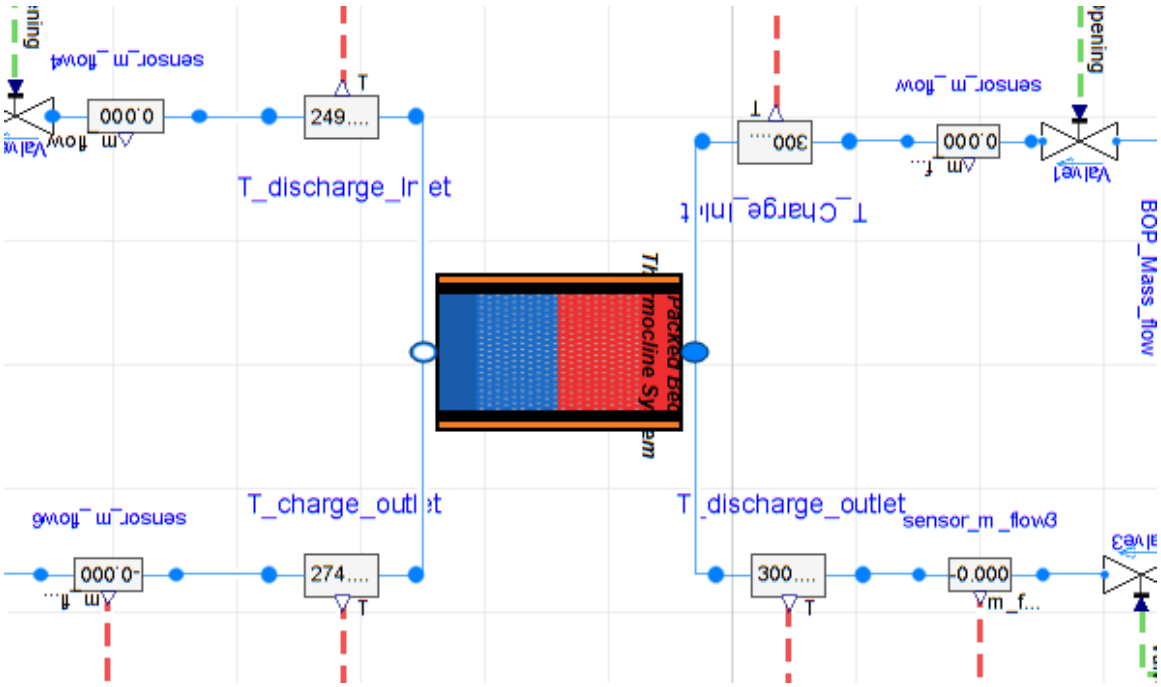

Figure 4. Enlarged thermocline in TEDS model, as shown in Figure 3.

The thermocline system can be seen in Figure 3, in addition to the wall and insulation components. The nodal representation of $i = 1$ to $i = N$ can be seen here, with this model having 200 nodes. It can store up to 200 kW thermal. The filler material for the single-tank packed-bed thermocline is 1/8 in. diameter Al_2O_3 (alumina) beads. Radial heat loss occurs, in addition to axial heat loss, through the tank walls and insulation. Heat losses are calculated via Fourier's law of heat conduction, as described in Equation (16), where the built-in Modelica models for cylinder conduction are used.

$$q'' = -\frac{dT}{dx} \tag{16}$$

The thermocline system is modeled using modified Schumann equations. More information about the Schumann equations can be found in References [16,17,18]. Table 3 shows the parameters used in the TEDS model. The Chromalox heater is the heat source for the loop in this model and was modeled using a multitransfer surface pipe. The medium is Therminol-66. The ethylene glycol HX is a generic distributed HX that acts as a heat sink/heat control unit in the loop. This type of HX has no inlet or outlet plenum considerations and is a generic shell and tube HX with discretized fluid and wall volumes. The tube-side contains ethylene glycol, while the shell side contains Therminol-66. The tube material for the HX is stainless steel 316. The heat transfer on both the tube and shell sides is calculated using a simple Dittus-Boelter correlation, as observed in Equation (17), where the correction factors are adjusted to meet predetermined heat transfer characteristics.

$$Nu = A \times Re^B \times Pr^C \tag{17}$$

Table 3. TEDS design specification [1].

Parameter	Value
Fluid Material	Therminol-66
Filler Material	Alumina
Wall Material	Stainless Steel 304
Insulation Material	Foamglass One
Porosity	0.25
Filler Diameter	0.00317 m (1/8 in.)
Tank Height	14.6 m
Tank Radius	7.3 m
Ambient Temperature	293 K
Nodes	200
Wall Thickness	0.051 m
Insulation Thickness	0.102 m
Charge Incoming Temperature	598 K
Discharge Incoming Temperature	498 K
Maximum Heater Power	200 kW
Nominal Full Heater Power	175 kW

The individual components of the HTSE are the SOEC, the recuperative HX, a hydrogen recycler, and a condenser. The full Dymola model of the HTSE can be seen in Figure 5 [15] where all of the modeling components inside the HTSE system can be seen, as well as the outside connections via ports, such as both the inlet and outlet air ports, the steam inlet port, the water-outlet port, the hydrogen-outlet port, and the electrical-inlet port. The SOEC is where steam is split into hydrogen. Other components show heat transfer of the inlet and outlet stream and how the inlet steam contribution is maintained. Condenser components can be seen in the dashed green box in Figure 5. The hydrogen recycler component is in the purple box, while the SOEC component is seen in the orange-dotted box in Figure 5. The SOEC is composed of 12 stacks, each of which contains 65 cells, for a total of 780 cells in the SOEC.

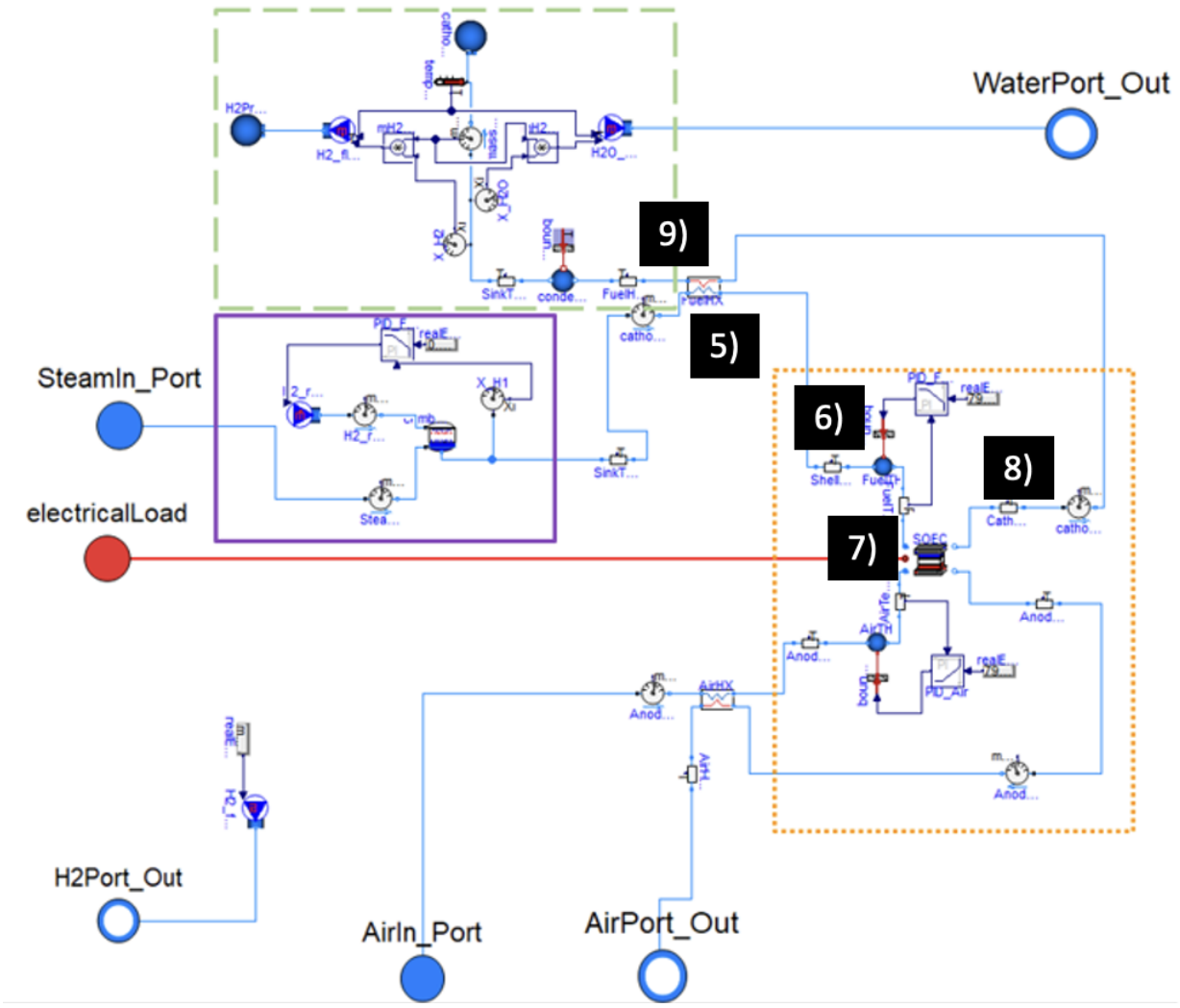

Figure 5. The HTSE and connection series location Modelica model. The box with the dashed green line represents the condenser, the box with the orange-dotted line is the SOEC, and the purple box shows the recycler.

The condenser is modeled as an ideal component splitter, which allows the individual species to be split in the incoming stream. The condenser allows for cooling of the hydrogen and condensation of the steam, which allows both to cool to 313 K. The component splitter measures the temperature and mass fractional flow of the individual species and provides those to two separate mass flow sources. The flow of the pure species goes to the outlet boundary ports. These outlet flows are the produced hydrogen and condensed water. Ten percent of the gas stream must be hydrogen in order to maintain a reducing environment for the cathode side of the SOEC. The hydrogen recycler component is made up of an ideal combiner, a proportional-integral-derivative (PID) controller, a hydrogen mass flow source, and mass-flow rate sensors. The PID controller controls the hydrogen mass flow source so that a 90% H_2O/10% H_2 molar fraction is maintained. The combiner mixes the incoming streams. In this case, the mixed streams are steam and hydrogen. The HTSE model must be connected to a direct current (DC) power source and fluid-boundary sources and ports. Table 4 shows the parameters used in the HTSE model.

Table 4. Design specification of HTSE.

Parameter	Value
Stack Cell Width	0.10526 m
Stack Cell Length	0.10526 m
Active Cell Area	0.01108 m^2
Number of Cells Per Stack	65
Number of Stacks	12
Total Number of Cells	780
Thermo-Neutral Voltage	1.283 V
Area-Specific Resistance	1.3 Ω-cm^2
Start Value on Inlet Pressure at Cathode	103,299.8 Pa
Start Value of Inlet Pressure at Anode	103,299.8 Pa
Stack Temperature	1063 K
Open Circuit Voltage (OCV)	0.93 V
Total Stack Voltage	1000.74 V

3.4 Scaling Ratio Determination

The objective of this section is to determine the initial and boundary conditions and transient data of the projected case based on the scaling objectives. For the initial and boundary conditions, the values are implemented into the TEDS and HTSE Dymola systems control to replicate the projected case simulations. The simulation results and projected transient data are compared to assess the scaling performance. The scaling objective is to: (1) accelerate TEDS and HTSE test cases; (2) match the amount of heat charge and discharge in the thermocline thermal storage system (TTSS) of TEDS; (3) increase the hydrogen production rate to achieve the same overall hydrogen production load (amount of hydrogen produced directly from the stack); and (4) perform these simulations without changing instrument type, structure materials, or geometry. To begin this process, the most restrictive system between the TEDS and HTSE Dymola models must be determined to decide which scaled equation ratio should be calculated first. After numerous considerations and attempts to change the system-control settings for TEDS and HTSE, it was discovered that the thermal transport fluid used in TEDS, Therminol-66, was most constrictive when trying to set fluid temperatures any higher than 673 K. As TEDS equations modeled in Dymola are written for single phase flow, the hot-side operating temperatures of over 673 K at 1.8 bar triggers a phase change. The gas properties of Therminol-66 are not provided and will break the simulation. While providing a 5 K margin for simulation-solution stability, the upper hot-side temperature limit is 668 K. This upper limit acts as a hard restriction to the TEDS scaling analysis because the maximum heat stored in the TTSS is now finite. If the amount of stored heat is to be matched, the test case maximum heat storage must be known and can be calculated using the applied mass flow rate, time of heat charge mode, specific heat capacity, and the corresponding storage temperature. The total test case heat storage is 662 MJ at an operating temperature of 598 K. Considering the test case total heat storage, test case mass of Therminol-66 fluid in TTSS, and the upper limit operation temperature of 668 K, the target upper limit mass for the projected case is 3361 kg as compared to the test case mass of 4158 kg. This is the result of following the scaling objective to match total heat storage. Abiding with the scaling objectives and scaled equations for TEDS in Table 2, the ω-strain ($\lambda_{A,th} = 1$) coordinate transformation scaled form from [23] is applicable, and the results can be given by:

$$t_R = \left[\frac{k}{\rho_{th} c_{P,th} T_{th,0}}\right]_R, \lambda_{B,th} = \frac{1}{t_R}, \lambda_{A,in} = \left[\frac{c_{P,out} T_{th,0}}{c_{P,th} T_{in,0}}\right]_R, \lambda_{A,out} = \left[\frac{c_{P,out} T_{th,0}}{c_{P,th} T_{out,0}}\right]_R, \lambda_{A,T_w} = \left[\frac{1}{T_{w,0}}\right]_R \quad (18)$$

Because the test case and projected case operating temperatures are known, the maximum accelerated time ratio is 0.855. In addition, because the mass ratio is 3361/4158=0.808, the mass flow rate ratio is $\dot{m}_R$=0.946. For the given scaling ratios in Equation (18), the calculated values are $\lambda_{B,th}$=1.219, $\lambda_{A,in}$=1.000, $\lambda_{A,out}$=0.996, and λ_{A,T_w}=0.959. To consider the amount of heat supplied by the shell and tube HX (the Chromalox heater in TEDS), the overall heat transfer can be calculated using the mass-flow rate, total heat-transfer time, specific heat capacity, and temperature difference. Assuming the cold-side temperature is maintained at 498 K, as was true for the test case, the overall heat-transfer ratio is 1.304, which yields an average power of 228.129 kW and a maximum power of 260.719 kW for the projected case.

For the HTSE system, the total amount of hydrogen must be conserved. This can be reflected in the established scaled equations in Table 2 by enforcing the ω-strain coordinate transformation to stack current ($\lambda_{A,I}$=1) and stack voltage ($\lambda_{A,V}$). Details of this type of scaling can be found in Reyes' 2015 paper [8]. This simplifies equations to derive the stack average temperature parameter of interest scaling form and nominal stack-voltage ratio as:

$$\lambda_{A,\bar{T}} = \left[\frac{V_0}{\bar{T}_0}\right]_R, \; V_{0,R} = \left[I\bar{T}_0 e^{\frac{10300}{\bar{T}}}\right]_R \tag{19}$$

Using the derived scaled equations in Table 2, applied ω-strain coordinate transformation, and scaling objectives to keep the geometry unchanged, the time ratio can be expressed in terms of SOEC equivalent heat capacity and stack current:

$$t_R = \left[\frac{C_{P,SOEC}}{I}\right]_R \tag{20}$$

Considering the time ratio is determined from the TEDS scaling analysis, and the change in heat capacity is minimal compared to stack current changes, the stack current can be approximated to be inversely proportional to the time ratio ($I_R \propto 1/t_R$). Assuming the change in heat capacity accounts for 10% of the stack current change for the given SOEC average temperature ranges, the stack current scaling ratio is I_R=1.287. Because the cathode- $\left(\pi_{ca} = \frac{2F\cdot\omega_{H_2O,in}}{n_c I}\right)$ and anode-feed factors $\left(\pi_{an} = \frac{4F\cdot\omega_{O_2,in}}{n_c I}\right)$ are maintained to be the same to ensure the balance between supply and consumption is untouched, the inlet flow rate scaling ratio for steam (ω_{H_2O}), hydrogen (ω_{H_2}), oxygen (ω_{O_2}), and nitrogen (ω_{N_2}) is equivalent to the stack current scaling ratio:

$$\omega_{H_2O,R} = \omega_{H_2,R} = \omega_{O_2,R} = \omega_{N_2,R} = I_R \tag{21}$$

From Table 2, the stack average temperature parameter of interest scaling ratio is $\lambda_{A,\bar{T}} = [V_0/\bar{T}_0]_R$. For both equations to be equivalent, the ratio of the hyperbolic sine must be 1 $\left(\sinh\left(I/2I_{ex,ca}\right)_R = 1\right)$. To ensure this is always true, the cathode exchange-current scaling ratio is equal to the stack current ratio ($I_{ex,ca,R} = I_R$). For the cathode exchange current scaling ratio of 1.287, the corresponding stack average temperature is 1079.300 K. Considering the test case operating-stack average temperature is 1063.150 K, the nominal stack average temperature-scaling ratio is 1.015. Now that the stack current and nominal stack average temperature-scaling ratios are known, the nominal stack voltage scaling ratio is 1.130. Using the nominal stack voltage scaling ratio and nominal stack average temperature scaling ratio, the stack average temperature parameter of interest scaling ratio is 1.113. For the remaining scaling ratios, some can be determined by considering operational conditions. Throughout the HTSE startup transient and steady-state operation, the SOEC inlet temperature, preheater inlet steam temperature, and ambient temperature are constant. Thus, the parameter of interest scaling ratios are 1 ($\lambda_{A,T_{in}} = \lambda_{A,steam} = \lambda_{A,amb} = 1$). Using the equations provided and calculated scaling ratios, the rest of the scaled ratios can be calculated but are omitted due to their having no relevance in the current HTSE Dymola model variable library.

3.5 Results and Discussion

For the purpose of this research, it is essential to have the following two components: (1) a test case simulation; and (2) a scaled case simulation based on the initial and boundary conditions determined in Section 3.4. In essence, the scaling process is recursive to converge to the optimal set of scaling equations. The scaling ratio determination, as shown in Section 3.4, is, by definition, a preliminary scaling analysis solely based on feedback from the test case data. A scaled case simulation using the preliminary scaling analysis acts as a reference to evaluate scaling performance. To investigate the scaling conclusions, Section 3.5.1 provides a visual and quantitative comparison of the TEDS and HTSE accelerated and projected cases. The differences between the accelerated and projected cases are:

- Accelerated Case: Using the derived initial, boundary, operating conditions, a Dymola simulation was run to generate the time reduced heat storage and hydrogen production conserved dataset.
- Projected Case: Using the determined scaled ratio values and generated test case date based on the initial, boundary, and operating conditions provided in Section 3.3, the projected (or predicted) dataset is calculated.

3.5.1 TEDS Test Case, Accelerated Case, and Projected Case Results

The TEDS test case had a maximum power of 175 kW thermal for the thermal energy system, while the maximum Chromalox heater power was 200 kW thermal. The maximum temperature was set to 598 K, and the minimum temperature was set to 498 K. The relative heater demand was set to 140 during 10,800 s – 14,400 s, but for the rest of the time it was set to 0. The demand from the balance of plant (BOP) is given as a function of time. For times between 3600 s and 9600 s, BOP demand was 0. For time durations of 0 s – 1800 s, 9600 s –10,800 s, and 14,400 s – 18,000 s, the relative demand was 100. Finally, between 10,800 s – 14,400 s, the relative demand was 140. It was run for a 5-h (18,000 s) cycle, during which both charge and discharge occurred. At 9600 s, the system switched from charging mode to discharging mode.

The temperature curves for the test case can be seen in Figure 6, where the scaling objective was to preserve the physical amount of heat stored at the end of the TTSS charging mode. Considering the increase in maximum heat generation to 260.719 kW from the Chromalox heater, decreased mass flow rate, and loop cold-side maintained at 498 K (i.e., the same as the test case), the charge- and discharge-mode simulations were conducted, as shown in Figure 7 and Figure 8, respectively. Starting from the charge mode comparison, the anticipated maximum temperature increase from 598 K to 668 K is reflected. Note that the starting temperature is 498 K, which is common between the accelerated and projected cases. The increased temperature difference preserves the amount of TTSS heat storage as the accelerated TTSS injected hot fluid mass is reduced to approximately 80% of the test case. This explains the reduction in charge-outlet temperature increase as the TTSS is only a relative fraction of the test case, and not enough time has elapsed to transport hot-line Therminol-66 fluid to the TTSS charge-outlet line. Because the discharge-inlet pulls Therminol-66 from the cold line, the temperature remains at 498 K.

The steps to calculate the DSS projected case are to: (1) determine the time ratio; (2) determine the parameter of interest scaling ratio (λ_A); and (3) use Equation (22) to postprocess the test case data. Reorganizing Equation (2) and plugging in Equation (1) gives the relation to calculate the projected data, given the prototypical system, for the test case:

$$\Psi = \Psi_0 \beta_{projected} = \Psi_0 \beta_{test} \lambda_A \tag{22}$$

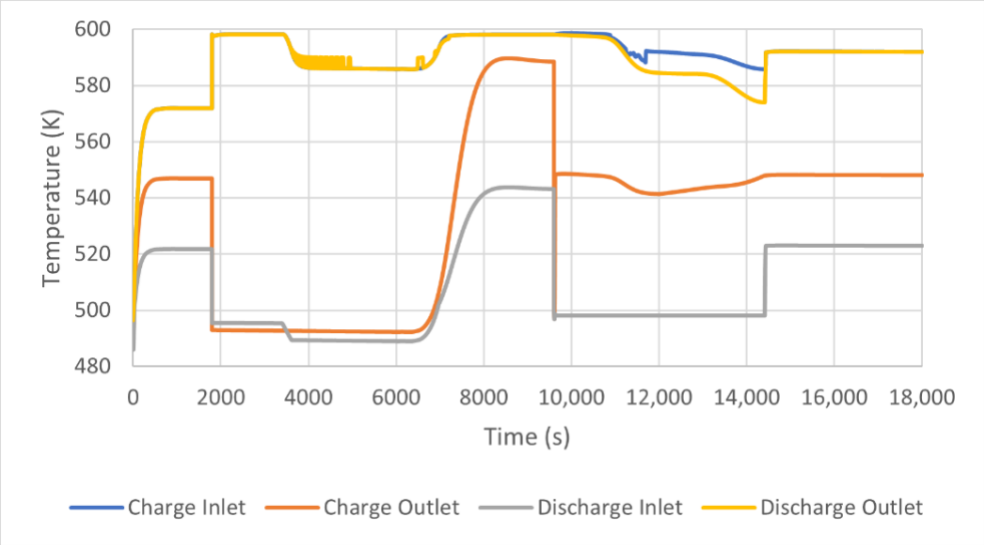

Figure 6. Thermocline temporal temperature profile.

Following the defined steps and using the preliminary scaling analysis, the projected case data were calculated for the TTSS inlet, outlet, centerline, and wall centerline temperatures, as shown in Figure 7 and Figure 8. From the first look, the charge outlet, discharge inlet, discharge outlet, charge centerline, discharge centerline, wall charge, and wall discharge temperatures show different features. For the charge-centerline, charge-wall, and all discharge temperatures, the timing and magnitude are offset. For the charge-outlet temperature, the data geometry indicates a large temperature increase after 5500 s starting from 403 K. This behavior can be explained by considering that all variables were normalized by the corresponding temperature values at the end of the charge mode, which for the projected case were around 9596.167 s and around 8477.034 s for the scaled case. The definition to be normalized is to adjust magnitudes that range around 1. The issue is the low temperature value relative to the reference value.

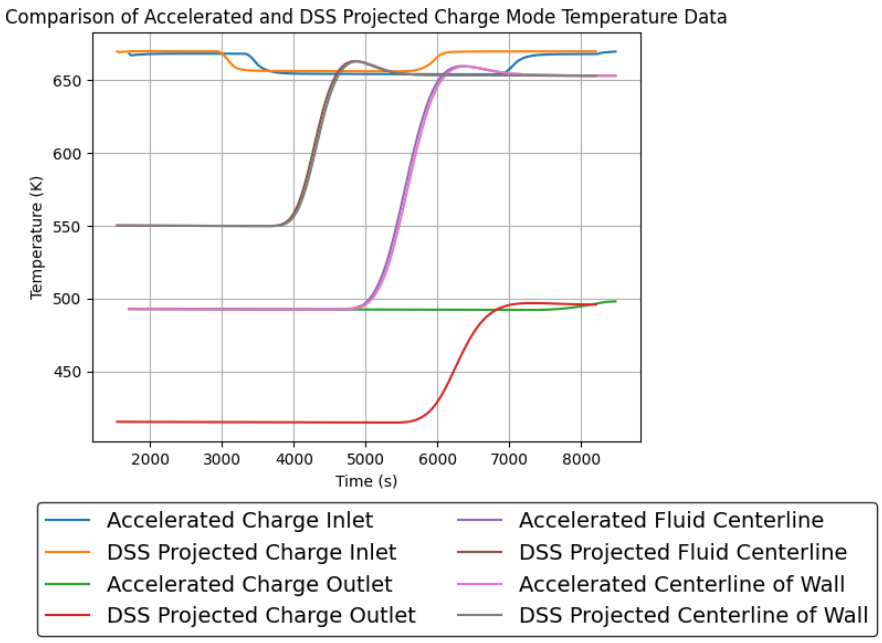

Figure 7. Comparison of accelerated and projected case charge mode core parameters.

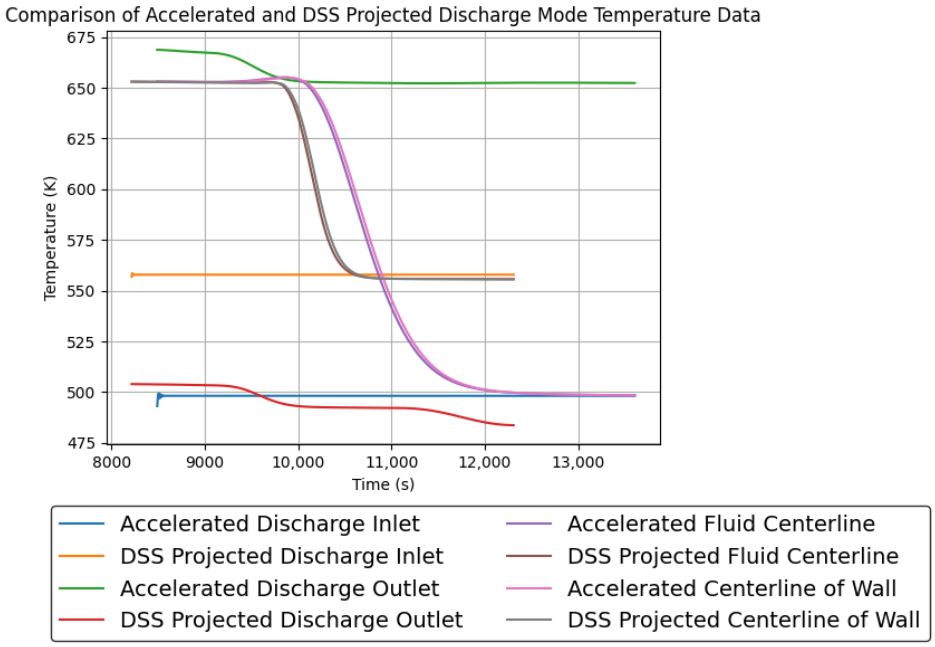

Figure 8. Comparison of accelerated and projected case discharge mode core parameters.

For example, consider the normalization at the initial charge time for both cases. For the scaled case, the reference temperatures were 668 K, 500 K, and 650 K for the charge-inlet, charge-outlet, and centerline temperatures, respectively, which correspond to the normalized values of 1.000, 0.991, and 0.842, respectively. For the test case, as given in Equation 22, the reference temperatures were 668 K, 582 K, and 581 K, respectively, which correspond to the normalized values of 1.000, 0.841, and 0.755, respectively. The difference in normalized values is mainly due to the relative magnitude of cold-side temperatures. As hot-side temperatures were upscaled, the cold-side temperatures remained the same, thus causing lower-temperature normalized values to differ significantly. Although from a scaling perspective, such decisions lead to scaling distortions, for operations, this is standard. If the cold-side temperatures were upscaled, this would suggest that the TTSS was pre-charged before the event and would not represent a case where the system is charged with the specified heat-storage amount. This adds complications because the parameter of interest scaling ratio for thermal terms is approximately 1 and, when applying Equation (22), the normalized values from the test case are inherited, outputting higher temperatures than were observed from the accelerated case.

As mentioned earlier, scaling analyses are recursive and are subject to modifications when less-compatible scaling decisions are made. In this case, the combination to normalize by the chosen reference value and leave the cold line temperatures resulted in distorted projections. Furthermore, although it may not be obvious, the discharge projected case, in terms of data geometry, performed better than the charge projected case. This suggests that there should be a separate scaling for charge and discharge modes. To modify the scaling analysis to account for the low temperatures and varied scaling performance between both operational modes, it is suggested that the normalizing method be changed. Regardless of what reference value is used whether it is a temperature value at some time or the temperature difference, the unscaled lower temperatures always trigger scaling distortions. One normalizing method that is capable of considering both maximum and minimum values is the minmax scaler used in machine learning. This is shown in Equation (23):

$$\mathrm{T}^{+} = \frac{T - T_{min}}{T_{max} - T_{min}} \tag{23}$$

Essentially, each data point is resized to range from 0 to 1 where 0 is the minimum value and 1 is the maximum value. When applying the minmax scale, Figure 9 and Figure 10 show the difference when considering the minimum and maximum values, regardless of temporal location. Magnitudes are now adjusted to be roughly the same, which is the correct normalization method for the type of assumptions and scaling decisions imposed. Because it was identified based on Figure 7 and Figure 8 that the necessity to separate the scaling analyses among the charge and discharge operations were emphasized, different time ratios were applied to achieve the results in Figure 9 and Figure 10. One remaining shortcoming from the modified scaling analysis is the different transient trends observed at certain time intervals for the charge and discharge modes. Charge-outlet temperatures were observed between 4000 and 6000 s for the charge mode and between 6500 and 8100 s for the centerline temperatures. Discharge-outlet temperatures were observed between 9300 and 12,500 s for the discharge mode and between 10,300 and 12,200 s for the centerline temperatures. The root cause of these distortions is the inadequacies in the modeling of the scaled conditions defined in Section 3.4. Figure 11 and Figure 12 show the test- and accelerated-case mass flow rates. Immediately, it can be seen that the control sequences between the test and scaled cases are different. Regardless of a change to the timing by a time ratio of 0.855, the on, off, ramping up, and ramping down do not behave as planned. This results in different fluid injection and ejection sequences, altering the data geometry and trends.

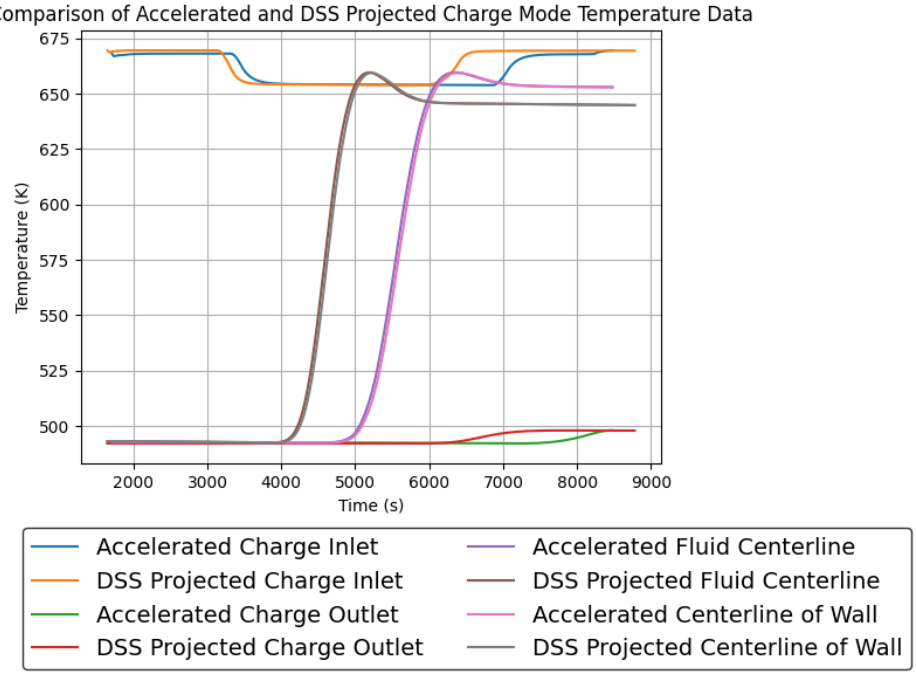

Figure 9. Comparison of the modified projected case and accelerated case charge mode core parameters.

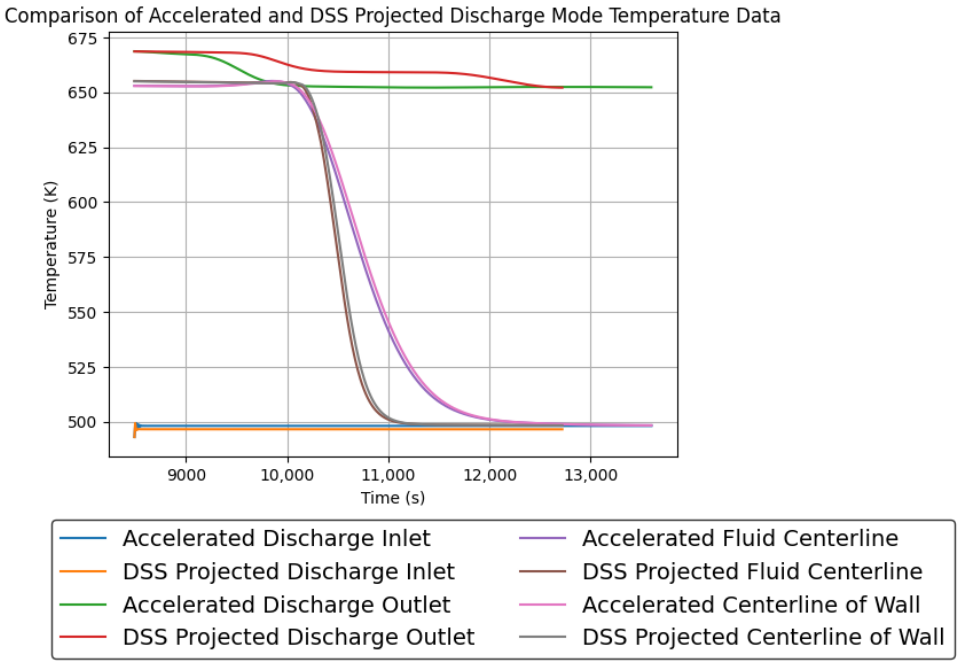

Figure 10. Comparison of the modified projected case and accelerated case discharge mode core parameters.

To emphasize the importance of the stated findings, consider an IES case where the stored heat is discharged for chemical processing. Chemical process plants are hard-conditioned systems that can only operate with specific temperature, pressure, and other conditions dependent on the given process. If the heat from thermal energy systems is used, precise system controls are required to ensure operating conditions are constantly met, even when transitioning from one heat source to another. The findings based on the applied scaling analysis amplify the control issues found in the scaled Dymola case. Without the scaling analysis, there would be difficulties on justifying the bridge between one case with the other and determining which transients require improvements. By having the capability to project data from the test cases, the ideal behavior based on the governing equations, scaling theory, and selected assumptions can be obtained and, to a certain degree, avoid costly retroactive facility changes as identified issues addressed during the pre-design phase. The recursive process of refining the scaling analysis will guarantee the validity. The current analysis is the first iteration to achieve this goal.

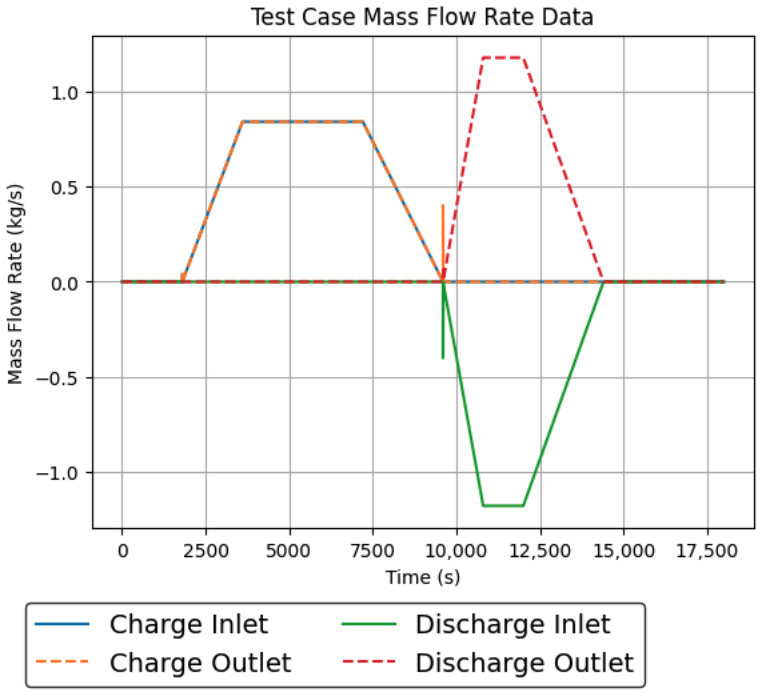

Figure 11. Test case mass flow rate control.

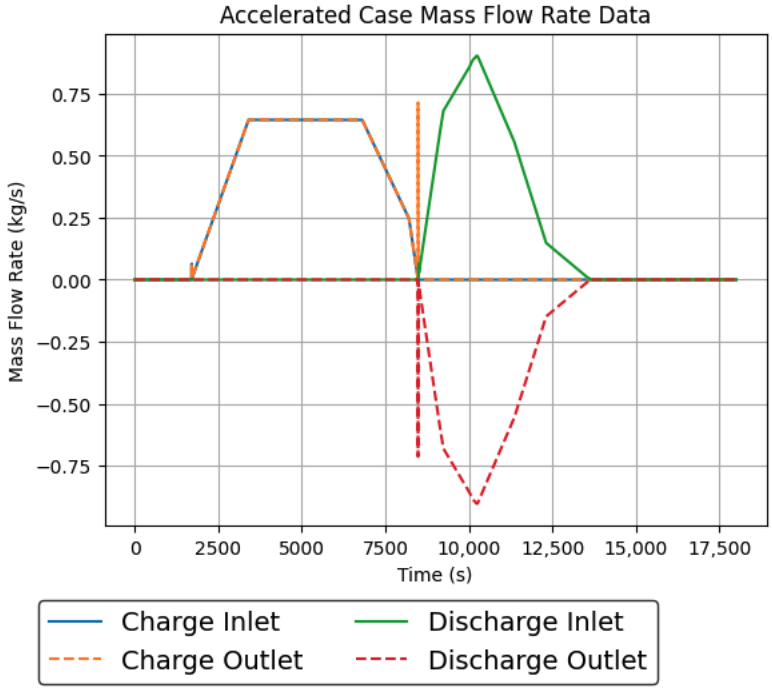

Figure 12. Accelerated case mass flow rate control.

3.5.2 HTSE Test Case, Accelerated Case, and Projected Case Results

For HTSE, the scaling objective is to increase hydrogen production by adjusting the stack current, voltage, and average temperature. Considering the 1.28 factor increase in stack current, 1.23 factor increase in voltage per cell, and significant increase in the stack average temperature to 1201.270 K, inlet

mass flow rates of 0.264 mol/s, 0.0293 mol/s, and 0.0520 mol/s for steam, hydrogen, and oxygen, respectively, were determined. Assuming the area-specific resistance remains unchanged, Table 5 shows the results of the accelerated case HTSE simulation. As stated in Section 3.3, the HTSE simulation is a time dependent steady-state problem. In reality, the startup of the stack over approximately 20 s should increase the applied voltage and furnace temperature until operating conditions are achieved for the specified stack current. Instead, the current Dymola HTSE model inversely solves for the stack current assuming thermal-neutral voltage and cell voltage based on furnace temperatures without delay feedback from the cathode- and anode-stack average pressures. The outcome is steady-state stack voltage and furnace temperature. For the applied scaling performance, the steam inlet mole flow rate, hydrogen inlet flow rate, and stack voltage increased as anticipated. However, the projected applied temperatures, oxygen mole flow rate, nitrogen mole flow rate, and stack current did not behave as in the scaled case simulation. Despite increasing the scaled case stack temperature to 1201 K, the applied temperatures did not increase significantly, and the possibility of mistakenly not reflecting other temperature conditions in other modeled components is high. For the scaled case nitrogen mole flow rate, oxygen mole flow rate, and calculated current, it was revealed by the Dymola model code that the physics were being calculated differently from the equation set used in Section 3.3. The modeled current density and stack power are given by Equation (24) [15]:

$$\mathrm{i} = \frac{\text{Operating Voltage} - \text{Open Circuit Voltage}}{ASR},\ \text{Stack Power} = \text{Operating Voltage} \cdot i \cdot A \tag{24}$$

Because the current density is calculated by subtracting the operating voltage from the open circuit voltage, and the area-specific resistance is unchanged by the scaling objectives stated in Section 3.4. The open-voltage reduced numerator values increase, and as a result, the stack current decreased compared to the test case values. The corrective action is to either: (1) change HTSE scaling equations to adopt Dymola models; or (2) modify the Dymola models to adhere to the set of HTSE equations introduced in Section 3.3. Although the cathode mole flow rates were not affected, a significant reduction in anode mole flow rates was observed. The HTSE findings in this case suggest that the applied scaling analysis was capable of discovering misplaced physics based on the projected results, as simulation model discrepancy is a large source of error.

Table 5. Accelerated and projected case values.

Output Parameter	Accelerated Case Value	Projected Case Value
Stack Inlet Temperature (<500 s)	1006.21 K	1092.68 K
Stack Outlet Temperature (<500 s)	1062.72 K	1281.62 K
Stack Steam Inlet Partial Pressure	65,078 Pa	65,078 K
Stack Hydrogen Inlet Partial Pressure	38,220.9 Pa	38,220 Pa
Stack Oxygen Inlet Partial Pressure	31,506.44 Pa	31,506.44 Pa
Stack Steam Inlet Mole Flow Rate	0.264 mol/s	0.264 mol/s
Stack Hydrogen Inlet Mole Flow Rate	0.0293 mol/s	0.0293 mol/s
Stack Oxygen Inlet Mole Flow Rate	0.0167 mol/s	0.0520 mol/s
Calculated Current (<500 s)	26.53 A	34.14 A
Stack Inlet Temperature (>600 s)	973.7 K	1069.9 K
Stack Output Temperature (>600 s)	1063.2 K	1281.6 K
Calculated Current (>600 s)	35.37 A	51.43 A

3.6 Data Projection Conclusion

In a first attempt to validate scaling activities under the IES program, multiple systems between TEDS and HTSE were scaled, and Dymola test cases were simulated. Based on the test case initial and boundary conditions and scaling objectives, the corresponding scaling ratios to calculate the accelerated case operating conditions and predict accelerated case simulation data were determined. The test case models were modified accordingly, and the scaled case models were simulated under the specified operating conditions. Concurrently, the scaled ratios applied to the test- and accelerated-case data were predicted (and referred to as the projected case). After comparing the projected and accelerated case data, several defects in the TEDS preliminary scaling analysis were discovered, and applied governing equation discrepancies were identified for the HTSE preliminary scaling analysis. To improve TEDS scaling performance, the normalization method was changed accordingly, and the scaling predictive capabilities were significantly enhanced. For HTSE scaling, two possible corrective actions were recognized; it was determined that further investigations would be required to fully comprehend the extent of the exhibited scaling distortions. The findings, based on measured separation for TEDS inlet, outlet, fluid centerline, and wall centerline temperatures, as shown in Figure 9 and Figure 10, suggest a mal-control sequence of the scaled Dymola simulation reflecting the conditions derived. Relatively high separations are observed around the charge to discharge mode transition. This is of great relevance to the large-scale and actual implementation of IES as precise system controls are required to ensure optimal coordination during flexible operations. As scaling processes are recursive and potentially require multiple reevaluations in order to converge to the optimal form, studies following this research will attempt to further improve the currently established scaling analysis to achieve facility demonstration quality. One aspect of note is that the simulations were conducted on TEDS and HTSE separately. Although the intent was to have an integral system simulation to observe the scaling analysis performance on the integral level, certain incompatibilities between the TEDS and HTSE models existed, delaying code development. In a case in which sufficient modifications are made, the same analysis will be conducted once more. To increase system similarity for TEDS and HTSE, scaling validation via facility demonstration is required. Finally, having the capability to project data from the test cases, the ideal behavior based on the governing equations, scaling theory, and selected assumptions can be obtained. For virtual IES emulations between facilities of multiple scales, the demonstrated capabilities can convert system-to-system signals enabling near-realistic IES operations and assist efforts to realize real-world IES.

4. SCALING INFORMED DESIGN

Advanced nuclear power plant (ANPP) technologies are expected to reshape the role of nuclear power in the energy industry. Forecasted to have an increased usage by the year 2050 [19], nuclear energy is also being proposed to serve electric and thermal loads for industrial decarbonization [20,21]. As ANPP technologies explore flexible operations to adhere to industrial processes, the requirements are well beyond normal base-load generations. Acknowledging normal operations of NPPs are favorable to near steady-state conditions—including core power, heat removal rates, and turbine operation—altering reactor normal operations to adjust to market, load-balance, and industrial process feedback inducing dynamic controls is increasingly challenging. For this reason, matching time-varying thermal-electric loads and ensuring minimal transients in the nuclear core, a heat delivery, storage, or augmentation system of high-density lasting long-durations are required. As an example, long-duration heat storage is a potential solution to couple an NPP to a pulp and paper manufacturing unit, which typically exhibits diurnal variations in its thermal load profile.

Although planning and designing a heat delivery, storage, or augmentation system suitable for coupling ANPP and industrial processes (in other words, IES) is a systems engineering problem, the methods used to identify and conserve the experienced phenomena from each system component are insufficient relative to the NPP design and certification process. NPP-coupled IESs that will emerge in the next 20 years are unique systems that will not only require prior pilot demonstrations, but justified system

designs based on previous successful operated components, design objectives, driving component phenomena, and scaling conclusions. The emphasis on applying scaling methodologies is to derive relations of system-scales to support or even determine operating conditions and component geometry. To achieve this degree of design, a method utilized by the United States (U.S.) Nuclear Regulatory Commission (NRC) is modified.

4.1 Methodology

The proposed method is based on a two-tiered approach using engineering and scaling methodology. This approach is adopted from NRC Regulatory Guide 1.203, "Transient and Accident Analysis Methods," which illustrates the process acceptable in developing evaluation models utilized for NPP design basis transient and accident behavior analysis [21]. The concept applied in this research is the Evaluation Model Development and Assessment Process (EMDAP) procedure. Four major elements are defined: (1) establish requirements for evaluation model capability; (2) develop assessment base; (3) develop evaluation model; and (4) assess evaluation model adequacy. These four elements are shown in Figure 13. For Element 1, it is required to specify a purpose, specify figures of merit (FOM), and identify the system, components, phases, geometries, and fields while ranking phenomena. This will define properties and characteristics of the structure and fluid of relative high concern in comparison to lower ranked phenomena. For Element 2, the main activities are specifying the objectives for the assessment base and applying the scaling analysis. As objectives are dependent on a case-by-case basis, for each individual objective, a separate scaling analysis will have to be applied. For Element 3, the evaluation model and structure is established. This will ensure the specified objectives and applied scaling analysis are corresponding and lead to meaningful simulations or experiments to assess the evaluation model process. Finally, in Element 4, the applicability of physical processes and the capability of field equations are determined.

The two-tiered approach is essentially Element 1, Element 3, and Element 4 for engineering and Element 2 for the scaling analysis. In the case of indirect two-tank heat storage systems, the engineering analysis will revolve over an intermediate heat exchanger (IHX), piping for liquid transfer, and storage tanks. Each system will have a form of governing equations covering mass, momentum, and energy, local phenomena such as flow and temperature conditions, and geometrical sizing. After defining the requirements and objectives of the evaluation model based on the engineering analysis, operational limits, and critical material limitations, the scaling analysis will be initiated to non-dimensionalize highly ranked phenomena, reorganize the dimensionless form in respect to identified critical parameters, and determine the scaled ratios when applicable. Although the EMDAP, as defined by the NRC, is geared towards nuclear reactor transient and accident analysis, the stated process for the two-tiered approach is the modified EMDAP for a two-tank heat storage system design basis, which is shown in Figure 14. The main difference is that they are planned for proof of design. As the necessity for integral effects test (IET) and separate effects test (SET) are meant for assessing code performance and validation, this aspect has been selectively omitted.

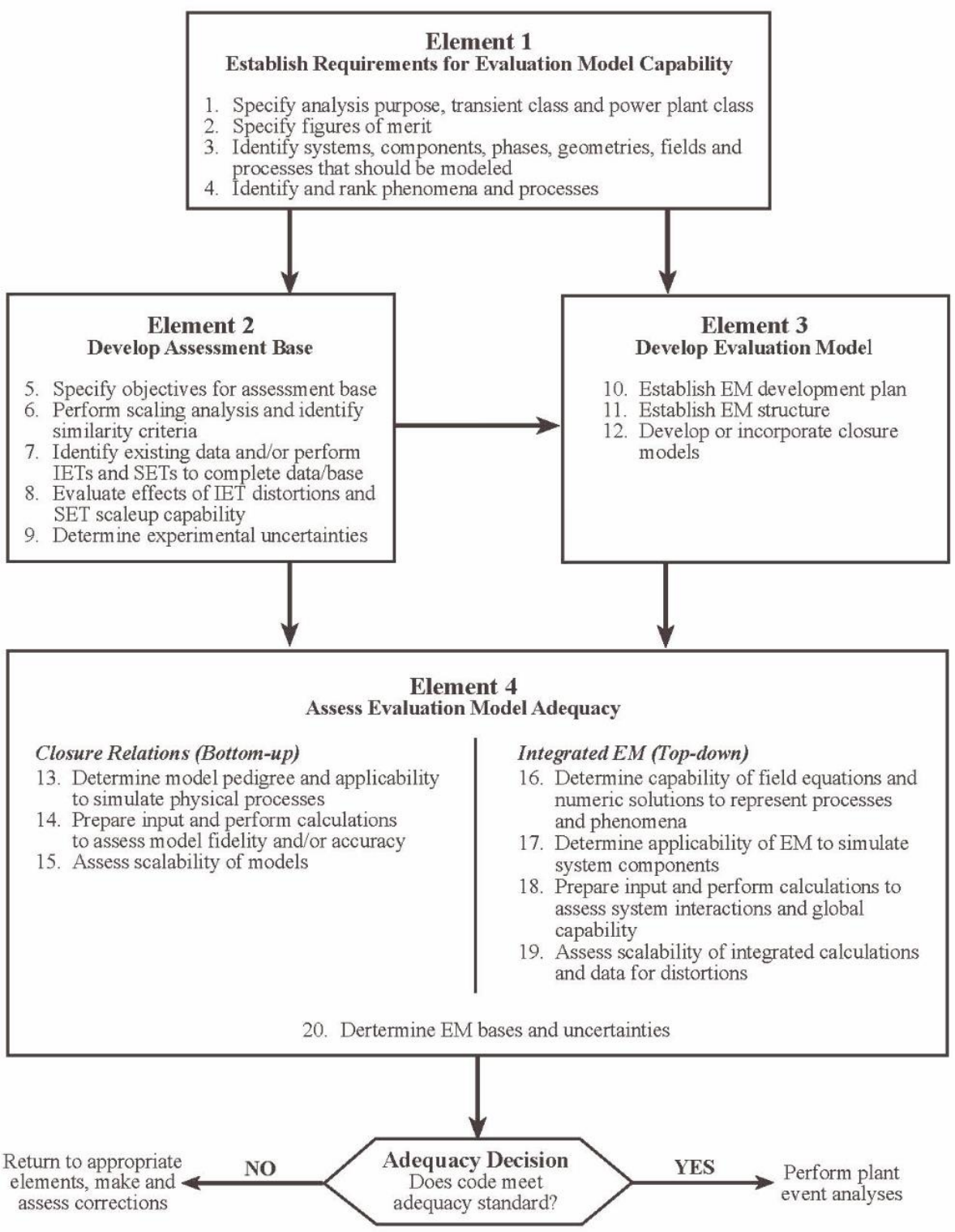

Figure 13. EMDAP, as defined by NRC Regulatory Guide 1.203.

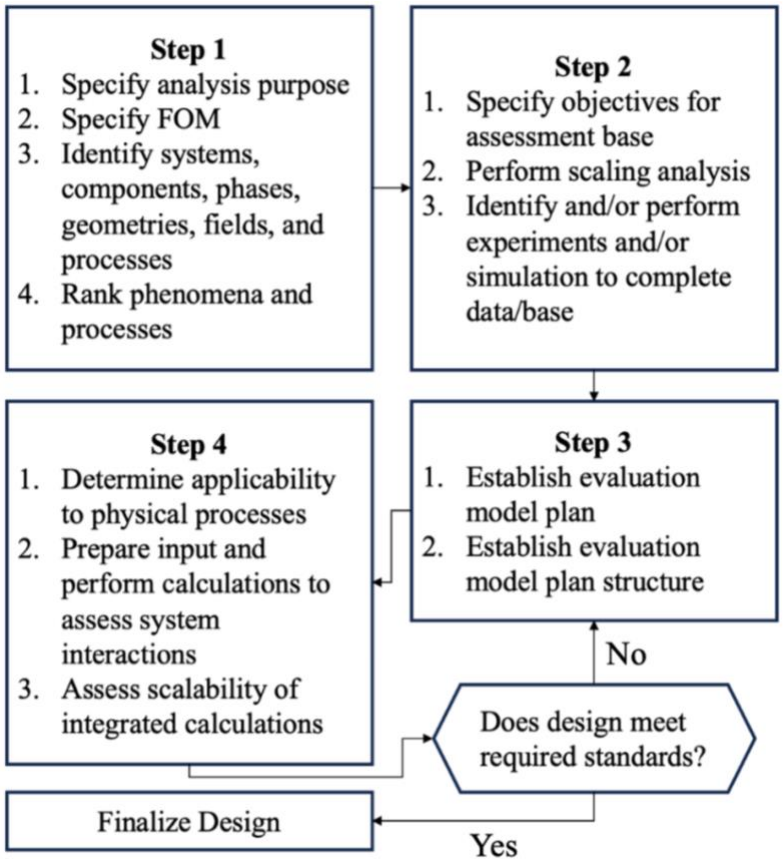

Figure 14. Modified EMDAP for a two-tank heat storage system.

4.2 Application – Indirect Two-Tank Heat Storage System

The application case to exercise the modified EMDAP, an indirect two-tank heat storage system was selected. The framework development to design indirect two-tank heat storage systems is based on the scaling analysis to discern the sizing of heat storage tanks when considering one or more tanks on each hot and cold side. For single-tank two-tank systems, the benefits are in the cost and maintenance as no extra piping or valves are required. However, in terms of thermal energy transport capabilities, multiple tanks have the advantage to remove one tank or more tanks and enable flexible means of thermal usage as the tanks can be delivered to other processes in an existing IES configuration. To initiate the design process, the steps for the modified EMDAP illustrated in Figure 14 are applied. Sections 4.2.1, 4.2.2, 4.2.2.2, and 4.2.3 follow the modified EMDAP. The major assumptions are that the type and size of IHX does not change, mass flow rate is at steady-state during charge and discharge mode, the heat storage fluid remained the same, and the refreezing of liquid temperature is neglected due to strip heaters triggered during freezing temperatures.

4.2.1 Step 1

The purpose of this analysis is to determine the required size reduction for multiple tanks that will conserve the flow and thermal storage properties of single-tank two-tank heat storage tanks while maintaining the same amount of heat storage. The first subsystem to consider is the heat source and heat sink IHXs. For any HX, a tube side and shell side exists to transfer thermal energy from high-temperature regions to relatively low-temperature regions. Thus, for both IHXs, two components exist: (1) a tube side and (2) a shell side. Common processes for the tube side and shell side are heat transfer relative to the flow conditions and HX type. The unique process is pressure-related, but the tube side is pressure drop

and the shell side is pressure loss. As the shell side can have numerous configurations based on the number and the position of the baffle plates, pressure change is characterized as a loss rather than a drop. For the ranking of IHX processes, the heat transfer coefficient and pressure reduction were regarded as having a significant impact to IHX performance. Since the IHX type and size is assumed to be unchanged, the effects are deemed negligible.

The second subsystem is the piping between the IHX and the heat storage tanks. The concerning phenomena can be discerned by acknowledging the environmental difference between the inner and outer portions of the pipes. The outer domain is solely driven by heat loss due to insulation installment preventing any heat transfer mode except for conduction. If the temperature difference between the pipe outer wall and the ambient temperature is large, a sufficient amount of insulation or strip heaters need to be installed accordingly producing a significant impact. Although the fluid type is another aspect that bounds the heat storage temperature and directly affects the total amount of energy storage, the applied assumptions allow for this to be negligible. For moderately impacted phenomena, pressure drop and viscous effects were identified. In most cases, the pipe sizes are chosen to be sufficiently large to prevent wall-induced flow resistance. On the other hand, the pipe sizes are equally sufficiently small enough in respect to pump horsepower limitations not to cause two-phase flow. If air or any gas is mixed in the pipe, this can lead to pump cavitation. Similarly, the appropriate pipe size will minimize pressure drop.

The third subsystem is the hot- and cold-side heat storage tanks. Common processes are pressure drop, viscous effects, and heat storage liquid type. Recalling phenomena ranking from previously specified subsystems, pressure drop and viscous effects are low impact, and heat storage liquid type is negligible. The lower impact evaluation is due to the larger diameter and length aspect ratio for tank designs. The process that differentiates both storage tanks in terms of levels of impact is the ambient tank heat loss. For the hot tank, higher temperatures are expected and contain larger risks of heat loss. This warrants a significant impact evaluation in comparison to the moderate impact for the cold tank. The phenomena identification and ranking table (PIRT) results of Step 1 are shown in Table 6.

Table 6. PIRT for indirect two-tank heat storage systems.

System	Component	Process	Period	
			1	2
Heat Source IHX	Tube Side	Heat Transfer Coefficient	H	H
	Tube Side	Pressure Drop	H	H
	Tube Side	Heat Exchanger Type	I	I
	Shell Side	Heat Transfer Coefficient	H	H
	Shell Side	Pressure Loss	H	H
	Shell Side	Heat Exchanger Type	I	I
Heat Sink IHX	Tube Side	Heat Transfer Coefficient	H	H
	Tube Side	Pressure Drop	H	H
	Tube Side	Heat Exchanger Type	I	I
	Shell Side	Heat Transfer Coefficient	H	H
	Shell Side	Pressure Loss	H	H
	Shell Side	Heat Exchanger Type	I	I
Piping between IHX and Heat Storage Tanks	Outer Domain	Heat Loss	H	H
	Inner Domain	Pressure Drop	M	M
	Inner Domain	Viscous Effect	M	M
	Inner Domain	Heat Storage Liquid Type	I	I

System	Component	Process	Period	
			1	2
Hot Side Heat Storage Tank	Outer Domain	Heat Loss	H	H
	Inner Domain	Pressure Drop	L	L
	Inner Domain	Viscous Effect	L	L
	Inner Domain	Heat Storage Liquid Type	I	I
Cold Side Heat Storage Tank	Outer Domain	Heat Loss	M	M
	Inner Domain	Pressure Drop	L	L
	Inner Domain	Viscous Effect	L	L
	Inner Domain	Heat Storage Liquid Type	I	I
Notes: Period 1: Charge Mode Period 2: Discharge Mode	Ranking: H: Significant impact to thermal storage design performance M: Moderate impact to thermal storage design performance L: Little effect to thermal storage design performance P: Probable but more knowledge required I: Negligible or not applicable			

4.2.2 Step 2

As described in Section 4.2, the objectives for the assessment base is to size heat storage tanks when considering one or more tanks on each hot and cold side while conserving the total amount of energy storage at the target storage time (e.g., four hours of heat storage). For the IHX and intermediate piping, the same conservation laws and governing equations in Table 2 were used and the derivation can be found in [13]. For the conservation laws specific to heat storage tanks introduced in Sections 4.2.2.1, 4.2.2.2, and 4.2.2.3, the resulting scaled equation is in Table 7. The heat storage tank conservation laws are the following sections below.

4.2.2.1 Mass

The conservation of mass characterizes the amount of liquid incoming and outgoing assuming no mass is generated or destroyed. Without assuming incompressible flow, the compressible conservation of mass in cylindrical coordinates is:

$$\frac{\partial \rho}{\partial t} + \frac{1}{r}\frac{\partial (\rho r v_r)}{\partial r} + \frac{v_\theta}{r}\frac{\partial (\rho v_\theta)}{\partial \theta} + \frac{\partial v_z}{\partial z} = 0 \tag{25}$$

where

ρ = liquid density

t = time

r = length in the radial direction

v_r = radial velocity

θ = azimuthal angle

v_z = axial velocity

z = distance in the axial direction

v_θ = azimuthal velocity.

By expanding the terms and ignoring the radial and azimuthal velocities, the differential density is:

$$\frac{\partial \rho}{\partial t} = -v_z \frac{\partial \rho}{\partial z} - \rho \frac{\partial v_z}{\partial z} \tag{26}$$

When considering the differential mass, the differential product of liquid density and volume (V) is used alternatively. As stated before, no mass is generated or destroyed. This leads to the mass flow rate being constant if no significant changes occur axially along the tank ($\dot{m}_{in} = \dot{m}_{out}$). Thus, the differential mass is equivalent to the mass flow rate. The difference between hot and cold tank mass flow rates is the exit flow from the IHX before each tank:

$$\frac{\partial m_c}{\partial t} = \frac{d(\rho_c V_c)}{dt} = \dot{m}_{IHX1} \tag{27}$$

$$\frac{\partial m_h}{\partial t} = \frac{d(\rho_h V_h)}{dt} = \dot{m}_{IHX2} \tag{28}$$

where subscripts c and h represent the cold and hot tanks. For subscripts $IHX1$ and $IHX2$, these describe the IHX for heat injection and extraction. $IHX1$ serves as the intermediate connection to the heat source, while $IHX2$ is the connection to the heat sink.

4.2.2.2 Momentum

The conservation of momentum, which is also known as the Navier-Stokes equation, expresses the convective, pressure, and viscous forces acting upon the defined control volume. Again, without assuming incompressible flow, the compressible conservation of mass in cylindrical coordinates is:

$$\frac{D(\rho v_z)}{Dt} = \frac{\partial P}{\partial z} + \mu \left(\frac{1}{r} \frac{\partial}{\partial r} \left[r \frac{\partial v_z}{\partial r} \right] + \frac{1}{r^2} \frac{\partial^2 v_z}{\partial \theta^2} + \frac{\partial^2 v_z}{\partial z^2} \right) \tag{29}$$

where P is the internal pressure and μ is the dynamic viscosity. By expanding the terms and ignoring the radial and azimuthal velocities, the differential velocity is:

$$\frac{\partial v_z}{\partial t} = -\frac{v_z}{\rho} \frac{\partial \rho}{\partial t} - \frac{1}{\rho} \frac{\partial P}{\partial z} + \nu \left(\frac{1}{r} \frac{\partial v_z}{\partial r} + \frac{\partial^2 v_z}{\partial r^2} + \frac{\partial^2 v_z}{\partial z^2} \right) \tag{30}$$

where ν is the kinematic viscosity. To consider the momentum balance, the differential Bernoulli's equation with head loss can be used to determine the relative magnitude of wall friction in respect to changes in axial velocity, dynamic pressure, and potential energy. Realizing the volumetric differential momentum can be expressed in terms of Bernoulli's equation, the momentum balance is expressed as the following:

$$\frac{d(\rho v_z V)}{dt} = -(\rho v_z A) v_z + (P_{in} - P_{out}) A + \rho g V - \frac{1}{2} \rho v_z^2 \left(\frac{fL}{D} \right) A \tag{31}$$

where

P_{in} = inlet pressure

P_{out} = outlet pressure

A = tank inner cross-section area

g = gravitational acceleration in the axial direction

f = friction factor

L = length of the tank

D = tank inner diameter.

4.2.2.3 Energy

The conservation of energy describes the modes of energy transfer into and out of the control volume including convective, conductive, generation, and heat dissipation. Again, without assuming incompressible flow, the compressible conservation of mass in cylindrical coordinates is:

$$\rho c_P \frac{DT}{Dt} = \nabla \cdot (k \nabla T) + \dot{q} + \Phi \tag{32}$$

where

c_P = liquid specific heat

k = thermal conductivity coefficient

T = liquid temperature

$\dot{q}$ = volumetric heat generation

Φ = heat dissipation.

By expanding the terms and ignoring the radial and azimuthal velocities, the differential temperature is:

$$\frac{\partial T}{\partial t} = \frac{\alpha}{r}\frac{\partial T}{\partial r} + \frac{\partial \alpha}{\partial r}\frac{\partial T}{\partial r} + \alpha \frac{\partial^2 T}{\partial r^2} + \frac{\partial \alpha}{\partial z} + \alpha \frac{\partial^2 T}{\partial z^2} + \frac{\mu}{\rho c_P}\frac{\partial v_z}{\partial r} - v_z \frac{\partial T}{\partial z} \tag{33}$$

Similarly to the momentum, the energy balance can be expressed by considering the heat transfer non-specific to mass for the entire heat storage tank. There are two separate modes to indirect two-tank heat storage systems—charge and discharge. Charge mode removes cooled liquid from the cold tank, which is heated by IHX, and injects heated liquid into the hot tank. On the other hand, discharge mode removes heated liquid from the hot tank, which is cooled by another IHX, and injects relatively low temperature liquid to the cold tank. Either mode requires one side of the tank to remove liquid while the other injects liquid. This essentially requires only one full tank worth of heat storage fluid to reduce initial capital costs. For this purpose, two separate energy equations would be assigned to describe each mode. Fluid injection is characterized by the mass flow rate and temperature difference denotes heat loss to ambient, considering conduction, radiation, and convection.

$$\text{Charge mode: } \begin{cases} \frac{\partial (m_h h_h)}{\partial t} = \dot{m}_{IHX1} h_{IHX1} - UA(T_h - Tamb\ ) \\ \frac{\partial (m_c h_c)}{\partial t} = \dot{m}_{IHX2} h_{IHX2} - UA(T_c - Tamb\ ) \end{cases} \tag{34}$$

$$\text{Discharge mode: } \begin{cases} \frac{\partial (m_h h_h)}{\partial t} = \dot{m}_{IHX2} h_{IHX2} - UA(T_h - Tamb\ ) \\ \frac{\partial (m_c h_c)}{\partial t} = \dot{m}_{IHX1} h_{IHX1} - UA(T_c - Tamb\ ) \end{cases} \tag{35}$$

4.2.2.4 Scaled Equations

Setting the parameters of interest to be liquid mass, liquid velocity, and liquid temperature, the corresponding dimensionless form is determined by dividing the nominal value and reorganizing to be explicit to the corresponding parameter of interest. By following the procedure in Section 2, Table 7 provides the derived relation (procedure can be found in Yoshiura et al.'s 2022 article [23]).

Table 7. Scaled subsystem processes for indirect two-tank heat storage systems.

Subsystem	Governing Equation Type	Scaled Equation
IHX	Overall Heat Transfer	$\left[\frac{1}{h_0}\right]\lambda_{A,Q} = \left[\frac{A_o}{A_i}\left(\frac{OD-ID}{k_w}\right)\right]_R = \left[\frac{A_o}{A_i}\left(\frac{1}{h_i}\right)\right]_R = \left[\frac{\dot{m}LN_P F_T OD}{\rho v_{T.0} Q_0 ID^2}\right]_R \left[\frac{1}{\ln\left(\frac{T_{shell,in}-T_{tube,in}}{T_{shell,out}-T_{tube,out}}\right)}\right]_R \left[T_{tube,out,0}\right]_R \frac{\lambda_{A,T_{tube,out}}}{\lambda_{A,v_T}}$
Intermediate Piping	Mass Conservation Momentum Conservation Energy Conservation	$\lambda_{B,\rho} = \left[\frac{v_{z,0}}{\Delta z}\right]_R \lambda_{A,v_z}\lambda_{A,\rho}, \quad t_R = \frac{\Delta z_R}{\lambda_A, v_z}$ $\lambda_{B,v_z} = \left[\frac{\nu}{r^2}\right]_R, \quad \lambda_{B,T} = \left[\frac{\mu}{\rho_0 T_0 c_P r}\right]_R \frac{\lambda_{A,v_z}}{\lambda_\rho}$
Heat Storage Tank	Mass Conservation Momentum Conservation Energy Conservation	$t_R = \left[\frac{\Delta z_R}{\lambda_{A,v_z}}\right], \lambda_{B,m} = \left[\frac{\dot{m}_{IHX}}{m_0}\right]_R, \lambda_{A,v_z} = \left[\frac{DL}{v_{z,0} t_R f L}\right]_R$ $\lambda_{B,v_z} = \left[\frac{P}{\rho v_{z,0}\Delta z}\right]_R = \left[\frac{(P_{in}-P_{out})}{\rho v_{z,0} L}\right]_R, \lambda_{A,\bar{v}_z} = \left[\frac{R^4\rho^2}{\dot{m}\mu}\right]_R$ $\lambda_{B,m} = \left[\frac{\dot{m}_{IHX} h_{IHX}}{m_0 h}\right]_R = \left[\frac{UA}{m_0 h}(T_{th}-T_{amb})\right]_R$

4.2.3 Step 3

The evaluation plan is to utilize the two-tiered approach from both engineering and scaling standpoints. In Section 4.2.2, the scaled equations for the relevant system components were determined. The engineering-side of the analysis is addressing critical design processes based on the developed PIRT shown in Table 6. The PIRT illustrates and ranks the different systems, components, processes, and periods built on state-of-start knowledge. For each process, two periods were considered—charge mode and discharge mode. There are five ranking levels: (1) significant impact (H); (2) moderate impact (M); (3) little effect (L); (4) probable (P); and (5) negligible or not applicable (I). The impacts are in respect to thermal storage design performance. For significant impact processes, the heat transfer coefficient and pressure loss of the IHXs, piping heat loss, and hot side heat storage tank heat loss were identified. Recall the objectives for the assessment base is to size heat storage tanks when considering one or more tanks on each hot and cold side while conserving the total amount of energy storage at the target storage time. In this case, the low and high temperatures, pressure conditions, and mass flow rates during charge and discharge periods are not changed and thermal energy transfer properties remain consistent between single-tank and multitank heat storage systems. For this reason, all heat transfer related significant impact processes are considered negligible. For moderate impact processes, the piping pressure drop and viscous effects, and cold side heat storage tank heat loss were identified. However, heat loss processes for previous reasons are negligible. For little effects, all are either pressure drop or viscous effects. In summary, the pressure drop (for IHX shell side, it is pressure loss) and viscous effects should be the main design point of this evaluation plan.

To evaluate pressure and viscous phenomena, characterizing the head loss will ensure the applicability of the current analysis. Throughout the design, the total mass flow rate is considered to be constant. For dynamic testing, the storage time is preferred to be about 4 hours. Mass flow rate is known to be the following:

$$\dot{m} = \rho v A \tag{36}$$

Ignoring compressibility, keeping temperature constant ensures the density is constant. For a system of constant pipe size, the controlling factor is velocity. The more velocity supplied; the more mass transferred per time step. As the pipe is extended, making different turns, or passing through components of different sizes, head loss is inevitable. Bernoulli's equation represents the overall evaluation of piping losses:

$$\frac{P_1}{\rho g} + \frac{1}{2}\frac{v_1^2}{g} + z_1 + h_{pump} = \frac{P_2}{\rho g} + \frac{1}{2}\frac{v_2^2}{g} + z_2 + h_{friction} \tag{37}$$

where

z = potential distance

h_{pump} = pump head

$h_{friction}$ = loss.

Subscripts 1 and 2 denote two separate locations in the system. The head loss is a sum of major and minor losses, which are associated with fluid viscosity and form loss:

$$h_{friction} = h_{major} + h_{minor} \tag{38}$$

The pressure loss in each segment is assessed by considering Poiseuille Flow (e.g., steady, axisymmetric, circular pipe). For given thermal and flow conditions, the pressure drop can be calculated:

$$(P_2 - P_1) = \frac{8\mu L\bar{v}}{R^2} \tag{39}$$

When considering the required pump head, different forms of losses can be characterized as insufficient pump horsepower, which will result in reduced mass flow rate and alter heat transfer properties. By reorganizing Equation (37) to be explicit to the pump head, the full form of loss is derived:

$$h_{pump} = \frac{8\mu L\bar{v}}{gR^2} + \frac{1}{2g}(v_2^2 - v_1^2) + (z_2 - z_1) + \left(\frac{f_D L}{D} + \sum K\right)\frac{v^2}{2g} \quad (40)$$

where

f_D = Darcy friction factor

K = form loss coefficient.

The execution of the evaluation plan will analyze the losses from each component to determine the relative order of magnitudes. In addition, the liquid velocity scaling analysis will be required as loss terms are associated to liquid velocity.

4.2.4 Step 4

To test the applicability of the two-tiered approach, Dymola [6,7] was selected as the system simulation tool to determine applicability to the physical processes in Table 6. The similarity of single-tank and multitank simulation data will be tested to assess scalability. Sections 4.2.6.1 and 4.2.6.2 describe the modeling done in Dymola.

4.2.5 Evaluation Plan

The evaluation plan will start from setting a reference test case to assess. The setup is a molten salt thermal energy storage (TES) system including a microreactor, an indirect two-tank heat storage system, and dumping heat into the atmosphere. For this purpose, the TES system will be divided into three subsystems—a charge loop, thermal storage tanks, and a discharge loop. To assess the degrees of head loss defined by Section 4.2.3, the reference heat transfer and storge fluid is molten salt. For the charge loop, the heat source IHX is between the microreactor (typically air-cooled) and charge-line performing at 2 MW_{th} duty. The incoming microreactor coolant is 750°C in a pressurized environment of 7 MPa running at 10 kg/s. Due to the specified duty, the outlet temperature is 571°C. The charge-line uses molten salt where the inlet cold liquid temperature is 267°C and the outlet hot liquid temperature is 420°C flowing at 15.66 kg/s in a slightly pressurized environment ranging from 120 kPa to 270 kPa. For the molten salt thermal storage tanks, the storage size is rated to handle the industry standard 4 hour storage, which is equivalent to 225,504 kg for both the hot and cold tank considering the mass flow rate of 15.66 kg/s is maintained. The mass variety is rooted from the molten salt density difference induced by separate operating temperatures. As is it can be deduced from the charge loop description, the cold tank storage temperature is 267°C, while the hot tank storage temperature is 420°C, which triggers a density difference of 75 kg/m^3. For the discharge loop, the heat sink IHX is between the discharge-line and the atmosphere (air-cooled radiator) performing at 2 MW_{th} to cool the molten salt to the cold tank operating temperature. Considering the inlet hot liquid temperature is 420°C and the outlet cold liquid temperature is 267°C flowing at 15.66 kg/s, the radiator fan revolutions per minute is adjusted to satisfy the target duty.

By applying the modified Bernoulli's equation to the piping and tanks, the head loss considering area change, pressure change, velocity change, and potential energy contributions were calculated, as shown in Table 8. As the pipe diameter increases, the magnitude of head loss is relatively decreased by orders of magnitude, which suggests the pipe-related loss is amplified by the smaller pipe diameters. However, the maximum calculated head loss is small at 30.358 mm. Assuming the heat source IHX is a variation of the shell and tube heat exchanger, the associated head loss keeping all the shell-side nozzle size, number of baffle plates, number of tubes, and number of shell passes the same, but changing the incoming and outgoing pipe sizing, were calculated to be 71.889 m at maximum and 71.828 m at average. Considering the shell flow path, head loss was calculated to be 71.889 m at maximum and 71.828 m at average. For the total head loss, the pipe, tank, and HX total maximum head loss is 72.230 m and total average head loss is 72.291 m. Judging from Table 8, the IHXs are the driving source of head loss by orders of magnitude.

Table 8. Tank, piping, and IHX head loss for three different intermediate piping sizes.

Tank, Piping, and IHX Head Loss (m)			
	Full Sized Tank	1/3 Reduced Sized Tank	IHX
Narrow Pipe (0.2 m)	0.0303577	0.0303463	71.745
Medium Pipe (0.6 m)	0.0001937	0.0001924	71.889
Wide Pipe (1.5 m)	3.3422e-06	3.11214e-06	71.889

When the single tank is being separated into multiple tanks, each flow is set to be in parallel ensuring the injection and ejection of liquid flow direction is aligned with gravitational acceleration. This also allows the head loss across each tank to be equivalent for each tank and is not the superposition as a tank configuration in series. Thus, the head loss of a single tank in place for the multitank case is sufficient to assess head loss from multiple tanks. One more aspect to consider is the type of flow based on the Reynold's number. Typically, turbulent flow consumes more energy than laminar flow due to vortex formations and extra mixing capabilities. This implies, as the fluid proceeds a certain distance through some structure, the chaotic behavior of turbulent flow requires more energy to sustain the current state. In the case for the molten salt heat storage system, if the theoretical piping length is around 50 ft from the heat source IHX, it is preferred to maintain a mass flow rate of 15.66 kg/s throughout the storage system loop. For the corresponding Reynolds numbers, the reduced tank hot side is at onset of turbulent flow (Re>2300) and may consume extra energy resulting in accelerated loss of flow. Since the reduced tank volume is one-third of the full tank, smaller tanks than the introduced reduced tank will be increasingly turbulent to maintain the prescribed mass flow rate.

Assuming the thermal properties are identical, the reduced tank velocity is times the squared diameter ratio of the full tank velocity by preserving geometrical similarity, as provided by Equation (41). As stated previously, the mass flow rate in each tank for the multitank configuration is designed to be equally distributed during molten salt injection and ejection. Thus, the sum of all individual tank mass flow rate should total the 15.66 kg/s to assess normal operations. Depending on how the volume is downscaled (e.g., height versus cross-section area), the change in cross-section area will potentially be downscaled significantly. The reduction of the tank diameter can be completely avoided if the height is shortened by $V_{full}/V_{reduced}$:

$$\frac{(\rho v A)_{full}}{(\rho v A)_{reduced}} = N \rightarrow \frac{v_{reduced}}{v_{full}} = \frac{1}{N}\left(\frac{D_{full}}{D_{reduced}}\right)^2 \tag{41}$$

By keeping the height/diameter ratio constant, Equation (41) is further simplified to Equation (42):

$$\frac{(\rho v A)_{full}}{(\rho v A)_{reduced}} = N \rightarrow \frac{v_{reduced}}{v_{full}} = \frac{1}{N}\left(\frac{D_{full}}{D_{reduced}}\right)^2$$

$$\left(\frac{D_{reduced}}{D_{full}}\right) = \sqrt[3]{\frac{\dot{m}_{reduced}}{\dot{m}_{full}}} \tag{42}$$

This selection of geometry is arbitrary since it only follows the mass flow rate balance. To further guide tank design, consider the average velocity parameter of interest scaling ratio ($\lambda_{A,\bar{v}_z}$). Using the momentum scaled relationships from Table 7, the average velocity parameter of interest scaling ratio is:

$$\lambda_{A,\bar{v}} = \left[\frac{R^4\rho^2}{\dot{m}\mu}\right]_R \tag{43}$$

From the analysis assumptions, the thermal properties are regarded to be matched between the single-tank and multitank system. In DSS, there are five scaling types: (1) 2-2 affine; (2) dilation; (3) β-strain; (4) ω-strain; and (5) identity [10]. For the given analysis, the same 4 hour storage time remains the same. This leads the time ratio to be t_R=1 and constrains the scaling type to be either dilation or identity. To conserve the mass transfer in and out the tank, $\lambda_{A,\bar{v}}$ is set to equal 1. Thus, the scaling type applicable is identity transformation and reveals the new relation between mass flow rate and tank radius:

$$\left(\frac{D_{reduced}}{D_{full}}\right) = \sqrt[4]{\frac{\dot{m}_{reduced}}{\dot{m}_{full}}} \tag{44}$$

4.2.6 Evaluation Plan Conclusion Demonstration

In Section 4.2.6.1, the Dymola setup demonstration test case for indirect two-tank heat storage charge and discharge transients are described. One important difference between the analysis introduced in Section 4.2.5 is that the heat transfer and storage liquid is Therminol-66 instead of molten salt. This decision was made to ensure indirect two-tank heat storage simulation accuracy precision, as the selected model from INL's HYBRID repository in GitHub used Therminol-66 as the test liquid. Sections 4.2.6.1, 4.2.6.2, and 4.2.6.3 provide more detail on the single-tank simulation geometry, operational conditions, and derived multitank dimensions.

4.2.6.1 Single-Tank Design from Existing HYBRID Repository

Figure 15 shows the Dymola model for the two-tank TES system. The most important components of this model are the hot tank and cold tank. Since the tanks need to exchange fluids at controllable rates, each tank has a pump to move the fluid through the control valve. After the valves, the fluid flows through one of two IHXs—one for charging and one for discharging—before entering the other tank. The storage medium flowing through the actual loop in this model is Therminol-66. The charging medium and discharging medium are both water. Although the charging and discharging media is the same here, it does not have to be this way. Initially, both tanks are 50% full, and the initial temperature is 240°C for both tanks.

Table 9 shows the parameters for the hot and cold tanks. The charging valve and discharging valve are both modeled as linear valves, which means they provide a pressure drop proportional to the mass flow rate and opening input. The linear valve model is adiabatic and neglects changes in kinetic energy. The inputs are the nominal mass flow rate and nominal pressure drop at full opening. The nominal flow rate at full opening for both the charging and discharging valve is 25 kg/s, while the nominal pressure drop at full opening is 1 bar. The pipes are transport delay pipes, pipe models that do not allow for mass and energy losses, but still account for frictional and gravitational pressure loss. The cross-sectional area of the pipes is 1 m^2, while the length is 10 meters. The pumps are centrifugal with ideally controlled speed. The discharging heat exchanger (DHX), or heat sink IHX, is modeled using a number of transfer units (NTU) HX, while the charging heat exchanger (CHX), or heat source IHX, is modeled using a shell and tube HX. The DHX calculates the total heat transfer as a function of internal heat generation in a control volume. This control volume has a source on one side and a sink on the other. It is for single phase flow. The medium in the tube is the storage medium, while the medium in the shell is the

discharging medium. There are five nodes in the CHX. The storage medium flows through the tube side, while the charging medium flows through the shell-side.

Table 9. Parameters for the hot tank and the cold tank.

Parameter	Value	Units
Max Level of Hot Tank	15	m
Hot Tank Cross-Sectional Area	50	m^2
Max Level of Cold Tank	15	m
Cold Tank Cross-Sectional Area	50	m^2

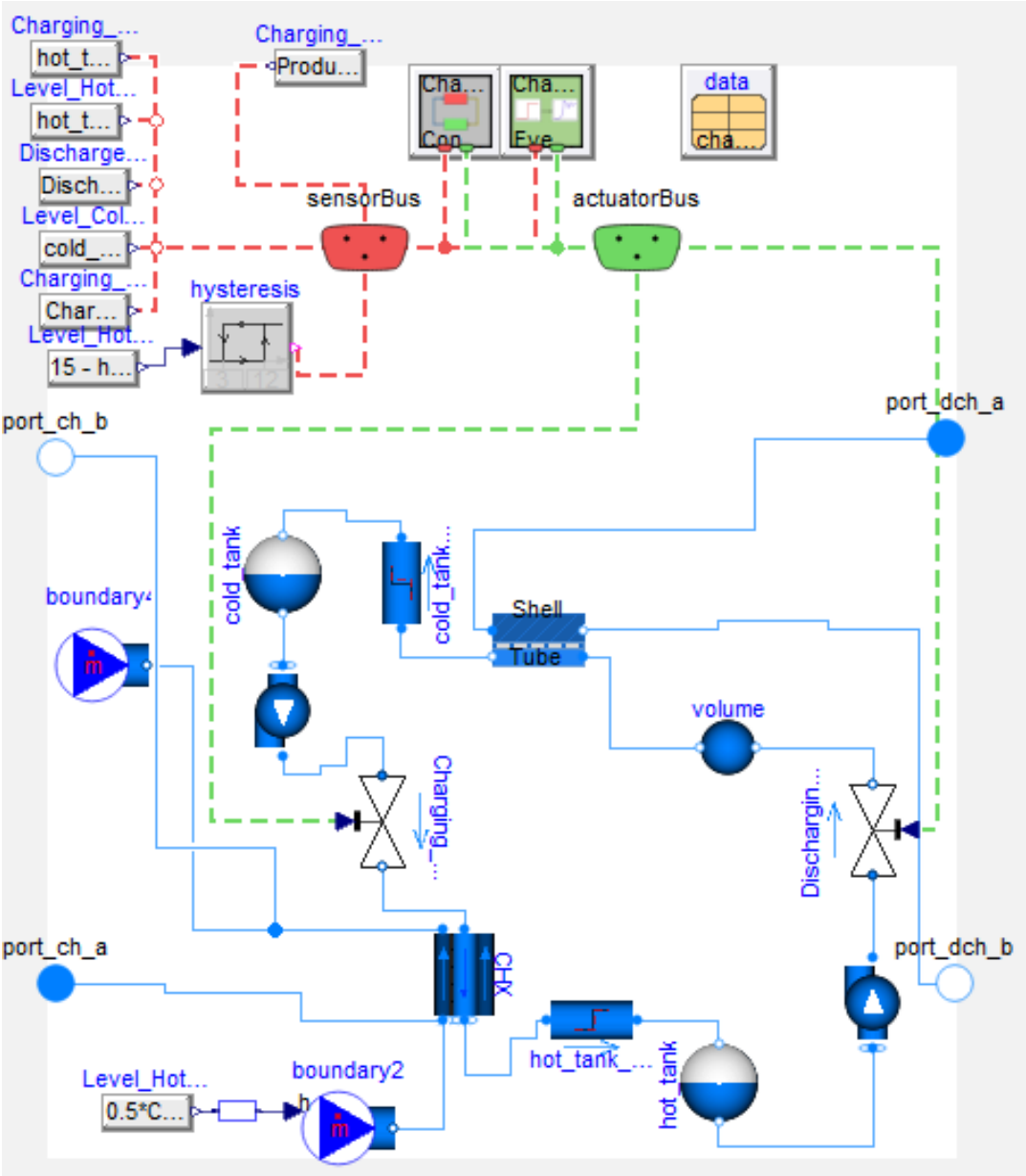

Figure 15. Single two-tank system model provided in HYBRID repository. NHES.Systems.EnergyStorage.SHS_Two_Tank.Examples.Build_Test.

4.2.6.2 Multitank Design

The multitank configurations were realized by using the flow multiplier function. As a result, mass flow rate reduction was observed at the given values from Table 10. The simple and scaling derived tank sizing can be calculated using Equation (42) and Equation (44). The results are shown in Table 11. As the number of tanks increases, the diameter difference between the simple and scaling results gradually increases. As a side-effect, the difference in tank height is increasingly affected. The larger the single-tank size, the more difference in geometry is exhibited. Keeping the same IHX, pump, and fluid temperatures in Section 4.2.6.1, the Dymola simulations for both simple- and scaled-tank geometries were run.

Table 10. Inputs for the flow multipliers.

Tank No.	Flow Multiplier Value	Mass Flow Rate (kg/s)
1	1	84.4
2	0.5	42.2
3	0.333	28.13333
4	0.25	21.1
5	0.2	16.88
6	0.167	14.06667
7	0.143	12.05714
8	0.125	10.55
9	0.111	9.377778
10	0.1	8.44

Table 11. Multitank design based on simple (Equation 42) and scaled (Equation 44) results.

Tank No.	Simple Diameter (m)	Simple Height (m)	Scaled Diameter (m)	Scaled Height (m)
1	7.978846	15	7.978846	15
2	6.332814	11.9055075	6.709383	10.6066
3	5.532223	10.40041877	6.062612	8.660253
4	5.026358	9.449407565	5.641896	7.499999
5	4.666057	8.772052927	5.335776	6.708203
6	4.390928	8.254817852	5.098029	6.123724
7	4.171005	7.841369122	4.9053	5.669467
8	3.989423	7.499999754	4.74425	5.3033
9	3.835829	7.211247615	4.606589	5
10	3.703452	6.962383022	4.486835	4.743416

4.2.6.3 Multitank Setup and Simulation Results

Flow multipliers were used to split the flow simulating the multiple two-tank set ups as shown in Table 10. Simulations were run for a one two-tank system up to ten two-tank systems. The flow multiplier component multiplies the flow by a capacity factor, which was equal to or less than 1 for the flow multipliers placed directly before the tank, and equal to or greater than 1 for the flow multipliers after the tank. Otherwise, this model is the same as the single-tank test case model. The placement of flow multipliers can be seen in Figure 16. Since the flow multipliers are placed before and after the tanks, the pump configurations are inherited from the single task case as described in Section 4.2.6.1. The major change in terms of simulation inputs are the tank geometry and hysteresis, which can be controlled by changing four parameters: (1) tank diameter; (2) tank default height; (3) minimum liquid level; and (4) tank upper margin. The minimum liquid level accounts for the required pump head for the given pumps used in the model. Since the multitanks are positioned and flow in parallel, the head height generated from an individual reduced tank is equivalent to the single-tank configuration. The tank upper margin accounts for the amount of height left empty to prevent liquid leakage. For the given tank storge design, injection and ejection of liquid is achieved by pumping to and draining from the bottom of each tank where injection and ejection lines are separated from each other. The total height of the tank is given by Equation (45).

$$\text{total height} = \text{tank default height} + \text{minimum liquid level} + \text{tank upper margin} \tag{45}$$

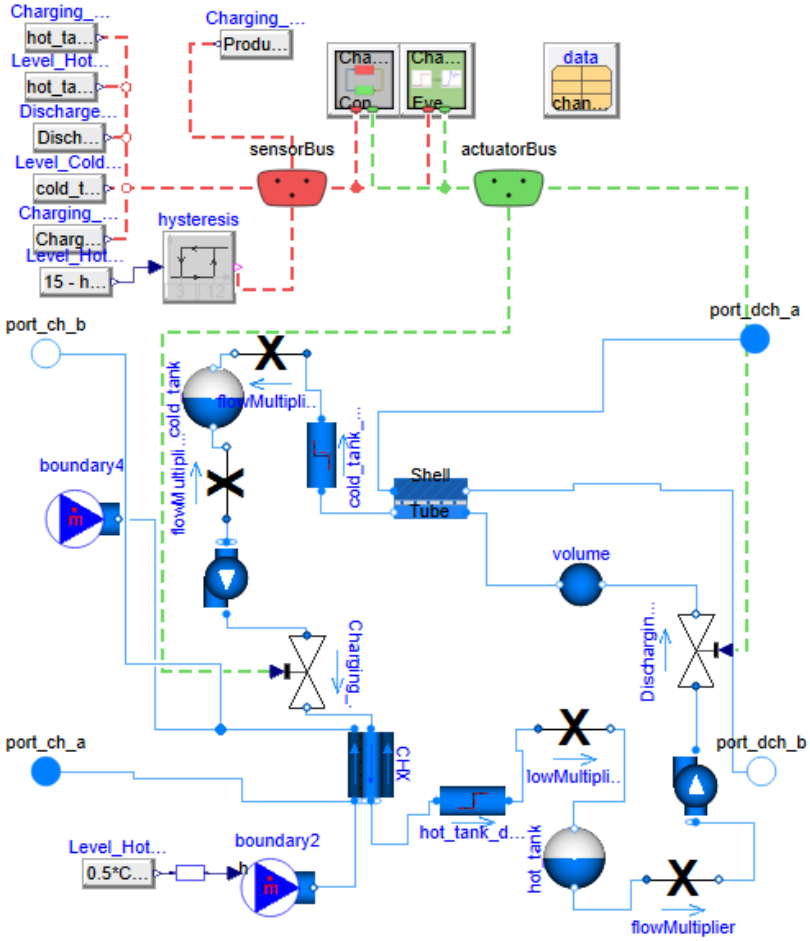

Figure 16. Multiple two-tank system model modified from the single two-tank system model in HYBRID repository. NHES.Systems.EnergyStorage.SHS_Two_Tank.Components.Two_Tank_SHS_System_Multiple_Tanks.

To ensure the amount of total heat stored in each tank is conserved, the tank height of each multitank system must have the required active heat storage volume. Recall that with more tanks, the more reduction in tank volume is observed. For example, the simple and scaled tank heights shown in Table 11 are the active heat storage values. Thus, the tank default height must be enough to satisfy the required active heat storage. Knowing the pump type and operating conditions will remain to be equivalent to single-tank configurations, the minimum tank level is maintained at the single-tank set value of 3 m for all multitank systems. To determine the tank upper margin for multitanks, consider the required height to be characterized using a timescale. This is analogous to the concept of light years as distance is used to characterize the amount of time light has traveled. For the single-tank tank upper margin, the value of 3 m was used. In terms of time, the tank upper margin is referred to as the time delay, where it is the time margin before the tank liquid level is high enough to cause liquid leakage. For the Therminol-66 density of 855.5 kg/m^3, tank area of 50 m^2, and mass flow rate of 84.4 kg/s, the single-tank time delay is given by Equation (46).

$$t_{delay} = \frac{\Delta h \rho A}{\dot{m}} = \frac{3\ m \cdot 855.5 kg/m^3 \cdot 50\ m^2}{84.4\ kg/s} = 1520.4\ sec \approx 25\ minutes \quad (46)$$

where Δh is the required tank upper margin. The major assumption to determine the tank upper margin is that all tank designs must contain the 25-minute time delay calculated value from the single-tank specifications. The new tank upper margin general expression is provided by Equation (47).

$$\Delta h = \frac{t_{delay} \dot{m}}{\rho N A_{multi}} \quad (47)$$

where N is the total number of tanks on a single loop; in other words, a three-tank multitank system will have three tanks on the hot side and three tanks on the cold side. Following the evaluation plan stated in Section 4.2.5, the multitank liquid density is kept constant for all systems at an operating temperature of 240°C. Using the Therminol-66 material property table provided in [24], the liquid density is still 855.5 kg/m^3. For the rest of the parameters, the values from Table 10 and Table 11 are provided. As a result, the calculated tank upper margin for the simple and scaled geometries are shown in Table 12. Running the single-tank, simple model designs from two to ten tanks, and the scaled design from two to ten tanks, the transient datasets for 4.32×10^5 s worth of repeated charge and discharge mode plots for simple/scaled hot tank inlet mass flow rate, cold tank inlet mass flow rate, hot tank liquid level, and cold liquid level are plotted in Figure 17, Figure 18, Figure 19, Figure 20, Figure 21, Figure 22, Figure 23 and Figure 24, respectively.

Starting from the hot tank inlet mass flow rate plots, the single-tank experiences 13 cycles of discharging and charging, which is the most as compared to the multitank results. Although the multitank mass flow rate values were indeed decreased by the flow multiplier shown in Table 10, the timing and amount of mass transfer (e.g., the integral area) did not follow the evaluation plan set in Section 4.2.5. If set properly, the number of charge and discharge modes would be the same 13 cycles as the single tank. Regardless, the integral area for each multitank case is equivalent to the single tank multiplied by the flow multiplier factor. Comparing both the simple and scaled designs in Figure 17 and Figure 18, Tank Number Case 2 is the only case where the same amount of cycles were observed. For the rest of the three to ten tank cases, the scaled designs experience more cycles than the simple designs. This is due to the shorter tank default height shown in Table 11. For the cold tank inlet mass flow rates, as shown in Figure 19 and Figure 20, the behavior compared to the hot tank inlet mass flow rates trends are different. The primary reason for cold tank inlet not returning to 0 (in other words, cold side pump never being shutdown) is the type of IHX modeled in the given simulation. The hot side pump is located before the CHX, which is a shell and tube HX, and allows well-behaved cyclic mass flow rate regulation. The cold side pump is located before the DHX, which is a NTU HX. NTU-based calculations rely on the heat capacity rates of the hot and cold liquids as the smaller of the two will be used to determine the maximum heat transfer. As a result, the cold side pump operation is constantly adhering to satisfy the DHX conditions while regulating tank levels. This discussion leads to the cold tank level plots in Figure 23 and

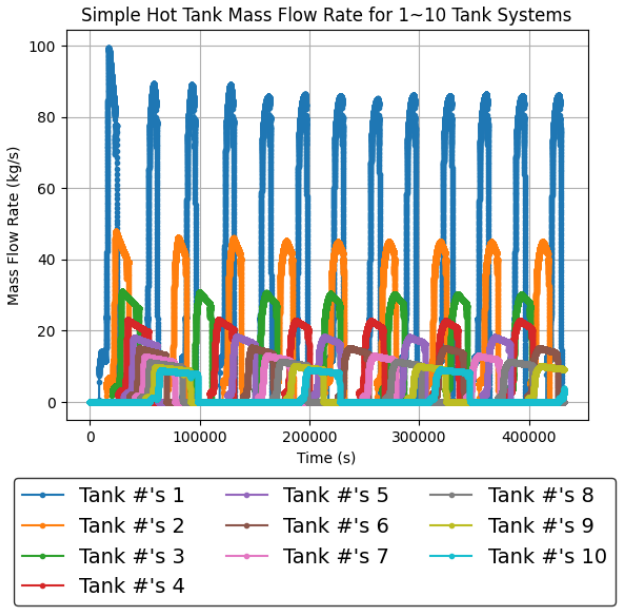

Figure 17. Simple hot tank geometry inlet mass flow rate for single tanks and multitanks.

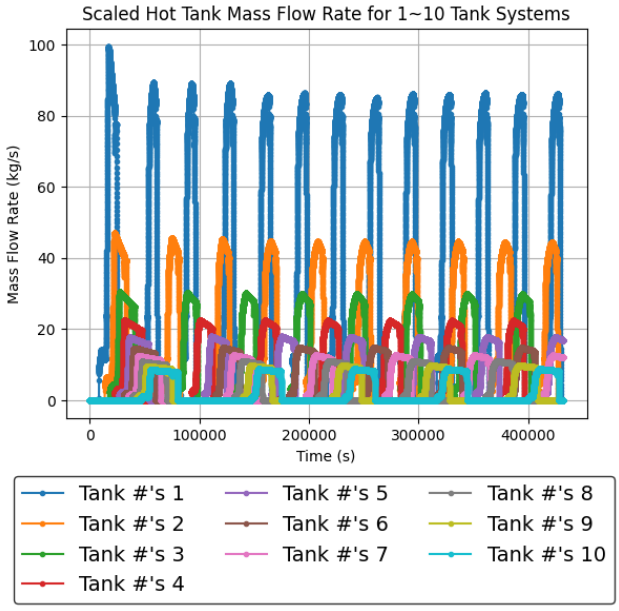

Figure 18. Scaled hot tank geometry inlet mass flow rate for single tanks and multitanks.

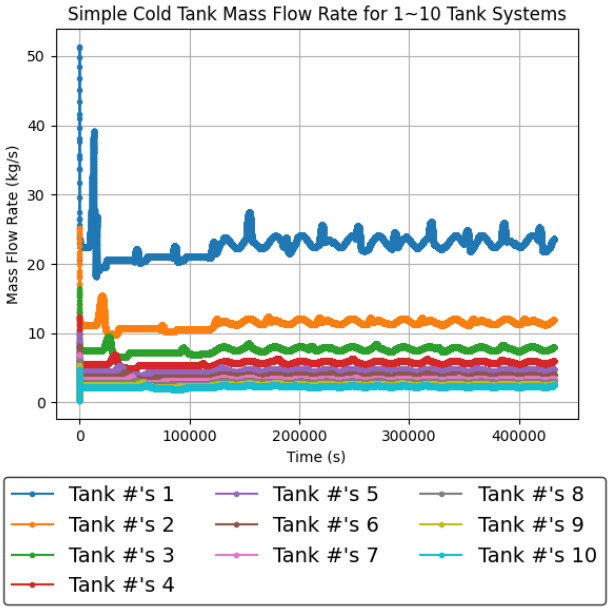

Figure 19. Simple cold tank geometry inlet mass flow rate for single tanks and multitanks.

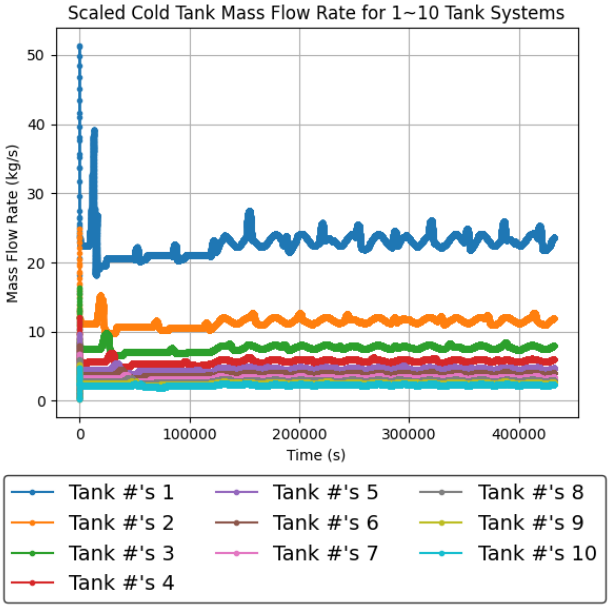

Figure 20. Scaled cold tank geometry inlet mass flow rate for single tanks and multitanks.

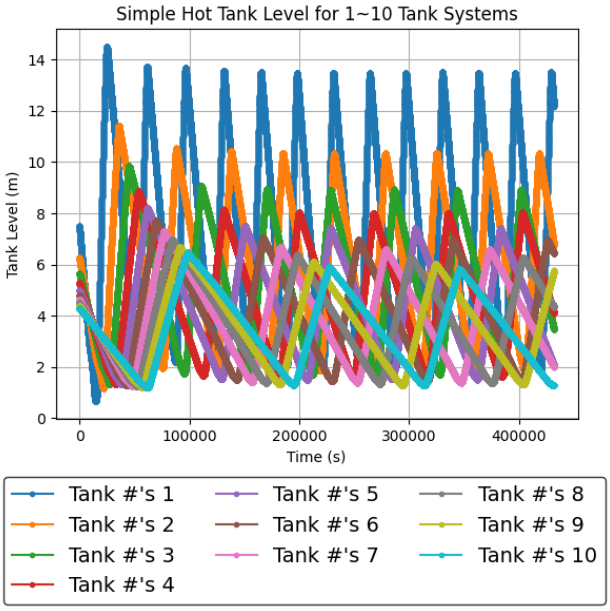

Figure 21. Simple hot tank geometry tank level for single tanks and multitanks.

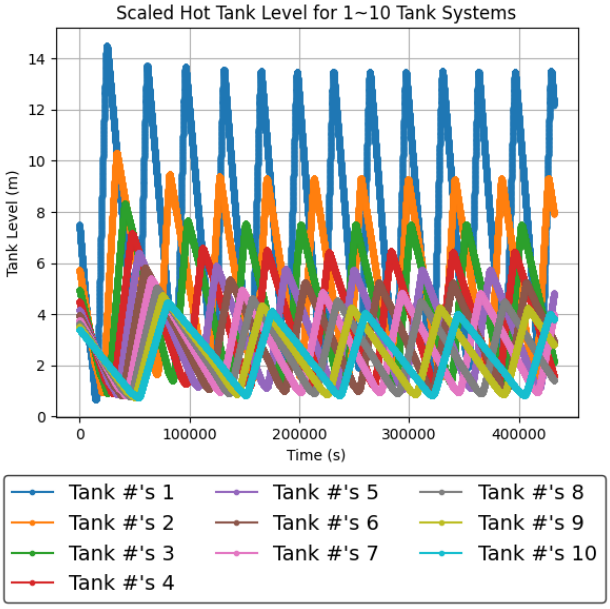

Figure 22. Scaled hot tank geometry tank level for single tanks and multitanks.

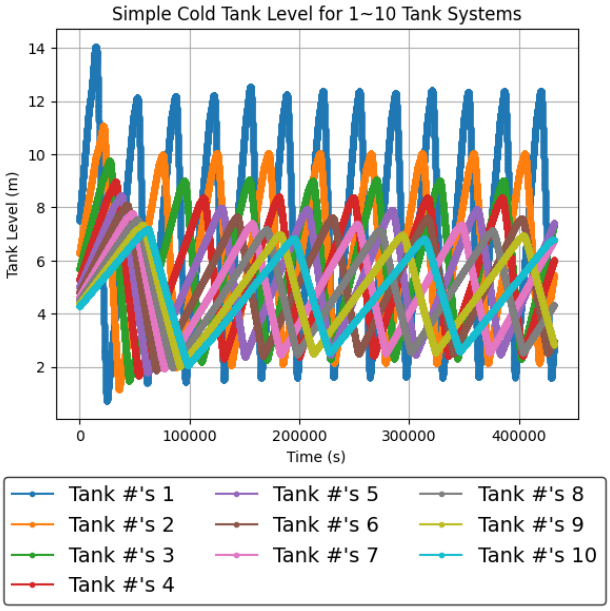

Figure 23. Simple cold tank geometry tank level for single tanks and multitanks

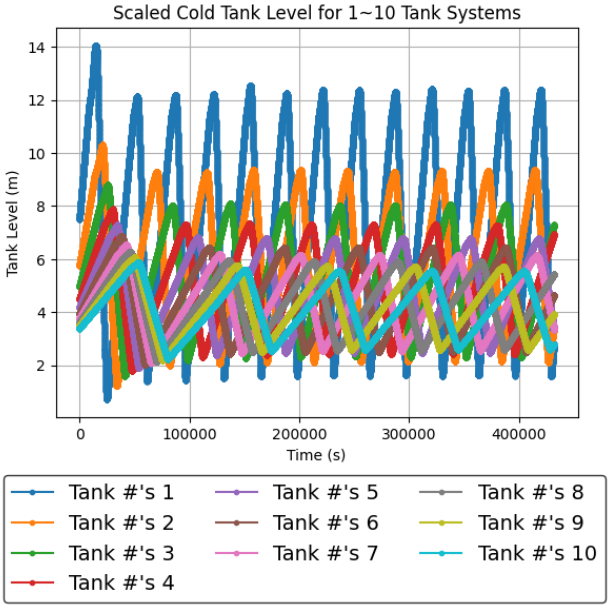

Figure 24. Scaled cold tank geometry tank level for single tanks and multitanks.

Table 12. Simple and scaled tank design upper margin and corresponding total tank height in meters.

Tank No.	Simple Tank Upper Margin (m)	Simple Tank Total Height (m)	Scaled Tank Upper Margin (m)	Scaled Tank Total Height (m)
1	3.00	15.00	3.00	15.00
2	2.38	12.53	2.12	11.49
3	2.08	11.33	1.73	9.93
4	1.89	10.55	1.50	9.00
5	1.75	10.01	1.34	8.37
6	1.65	9.61	1.22	7.90
7	1.57	9.28	1.13	7.54
8	1.50	9.00	1.06	7.24
9	1.44	8.76	1.00	1.00
10	1.40	8.58	0.95	6.79

Figure 24. The simple and scaled design tank level transients follow the corresponding mass flow rate behavior and set hysteresis. The hysteresis setup is for tank levels not to go below the minimum tank height or above the tank upper margin. From Figure 23 and Figure 24, the hysteresis is well controlled within the set boundaries. For the number of cycles, it matches the behavior seen in the hot tank inlet mass flow rate plots.

Although the cold tank inlet mass flow rates do not give insight to the cold tank levels, they do function to produce well-behaved cold tank level control. Lastly, for the hot tank levels, they are similar to the cold tank level behavior, but with a reflection regarding the time axis.

Judging from the inlet mass flow rate and tank level plots, the similarities between the single-tank and multitank results are not obvious. In terms of transients, the simple and scaled design trends indicate a strong resemblance to each other by not revealing which method represents the single tank in detail. To qualitatively evaluate which design is superior, the single-tank and multitank datasets were postprocessed using Equations (4), (5), (6), (7), and (8). To visualize the dataset effectively, the datasets are plotted using the phase diagram as introduced in Figure 2. When processes are ideally matching, the datasets will overlap. After postprocessing to calculate for the parameter of interest (β) and normalized agents of change ($\widetilde{\Omega}$), the phase diagrams are shown for a single cycle. A cycle is defined as a process to return to its original value. This is to enable easier visual inspections and avoid data congestion. This is especially important for postprocessed parameters such as the normalized agents of change, as high-order derivatives may range to extreme values. To further ease the visual inspections, the dataset was separated at local minima and maxima due to the nature of calculating the process time. Recall from Equation (5), the process time is calculated by dividing the parameter of interest by the agents of change. If the agents of change is 0, this will create undefined values and errors in computation while attempting to determine the integral of the temporal displacement rate (D). The dataset was separated into three identifiable transients: (1) the first half discharge; (2) the one full charge; and (3) the second half discharge. For the single-tank and all multitank datasets, the location of local minima and maxima were different. By selecting the appropriate cycle start and end time for each case, the location of local minima and maxima were determined. For data representation, the hot tank level phase diagrams were chosen. The primary reason for this choice was because the amount of stored fluid dictated the amount of stored energy at a given time. If the tank levels are similar in the phase diagram, then the geometry of the multitank design is justified. Since the cold tank level data reflects the hot tank levels about the time axis, showing both hot and cold tank levels would be redundant. For the hot tank level, the first discharge mode phase diagram,

Figure 25 and Figure 26 show both simple and scaled design hot tank level postprocessed parameter distributions.

Although the log-scale magnitudes vary significantly, it can be seen with every tank size for both the simple and scaled designs that the trends follow the single-tank data. The basic trend observed was tank drainage starting from a partially filled tank with parameter of interest values ranging from $0.5 < \beta < 0.6$ and all ending at near 0, which is the value at minimum tank level according to the normalization method used by Equation (23). For the simple design, Tank Number Cases 4 and 10 were relatively farther than the other cases in reference to the single-tank data. For the scaled tank design, Tank Number Cases 8 and 9 were relatively farther as well. For the hot tank level charge mode phase diagram, Figure 27 and Figure 28 show both the simple and scaled design hot tank level postprocessed parameter distributions. The trends seen in this transient were full tank injection starting from the minimum value ($\beta = 0$) and ending at the maximum value ($\beta = 1$). Surprisingly, the tank numbers that exhibited relatively high distances did not change for the simple or scaled designs. Nonetheless, for the hot tank level second discharge mode phase diagrams in Figure 29 and Figure 30, the outstanding cases remained the same. In terms of trends, they used the same process as the first discharge mode except the starting location is from the maximum tank height to the initial tank height. The global trend for all three transients was that the level changes were near linear as the normalized agents of change remained mostly flat. For the relatively close cases, Tank Number Cases 5, 6, 8, and 9 were best for the simple design and Tank Number Cases 4, 5, 6, and 10 were best for the scaled designs.

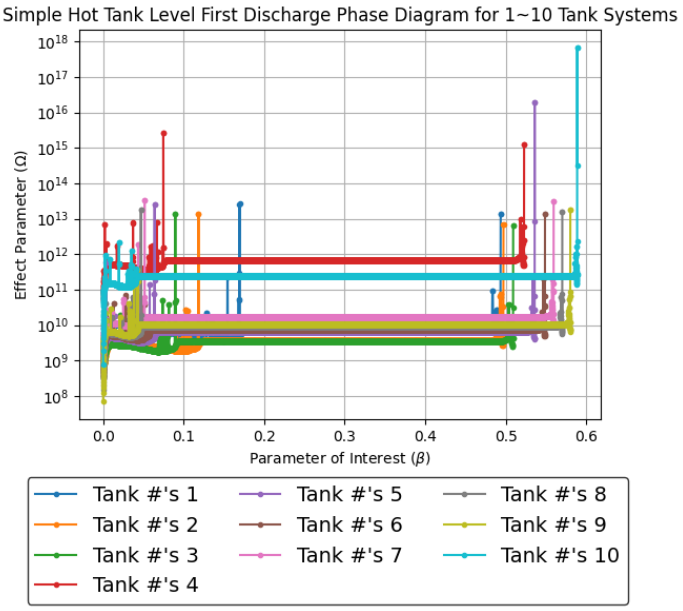

Figure 25. Simple cold tank geometry tank level first discharge mode phase diagram for single tanks and multitanks.

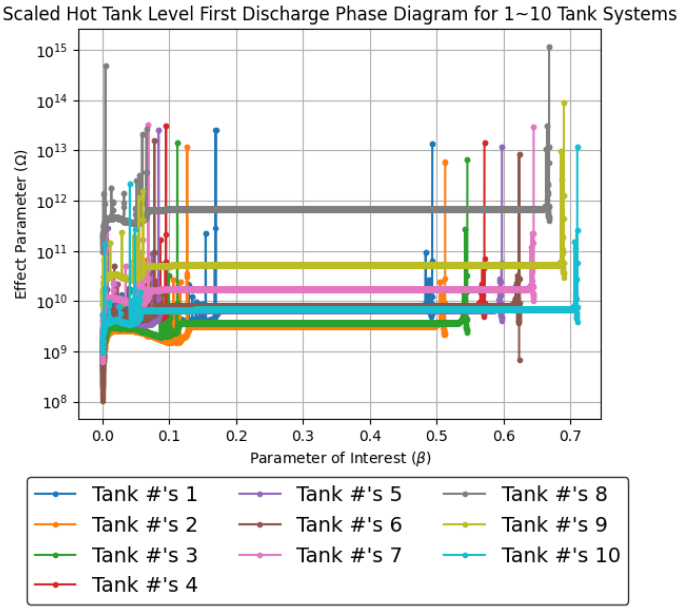

Figure 26. Scaled cold tank geometry tank level first discharge mode phase diagram for single tanks and multitanks.

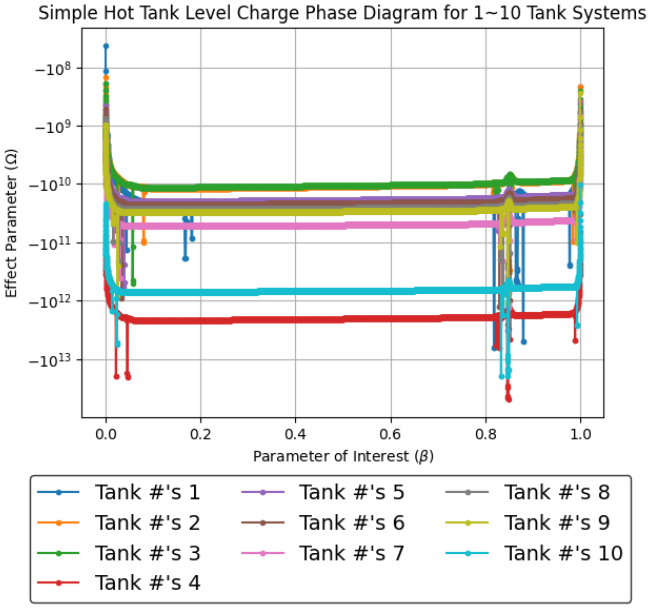

Figure 27. Simple cold tank geometry tank level charge mode phase diagram for single tanks and multitanks.

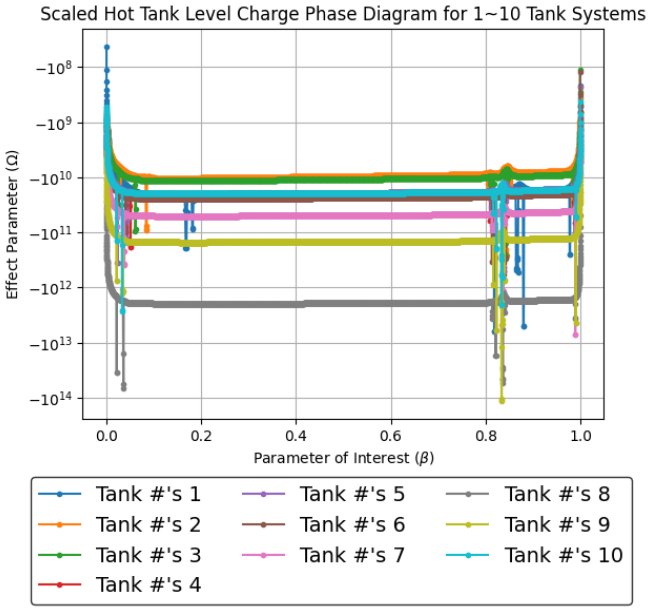

Figure 28. Scaled cold tank geometry tank level charge mode phase diagram for single tanks and multitanks.

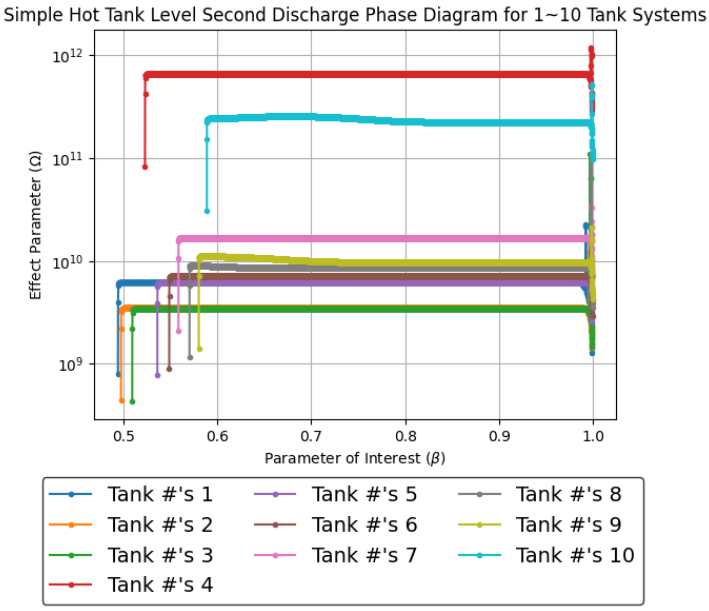

Figure 29. Simple cold tank geometry tank level second discharge mode phase diagram for single tanks and multitanks.

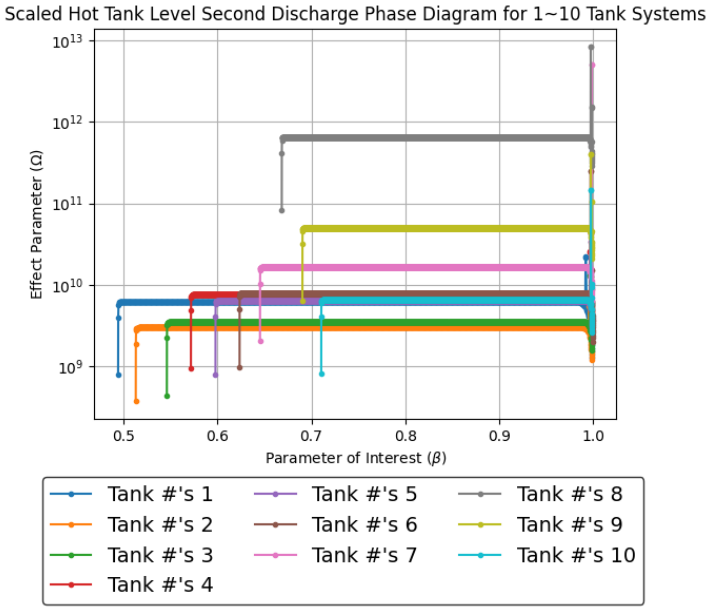

Figure 30. Scaled cold tank geometry tank level second discharge mode phase diagram for single tanks and multitanks.

To quantitively assess design performance, the DSS metric introduced in Section 2 was used. Posing the single-tank simulation results as the prototype dataset and multitank simulations as the model results, the global difference between the single-tank and multitank datasets using Equation (15) was calculated. Despite being capable of assessing the local metric at each point that were equivalent at the determined normalized process time using Equation (14), the objective of using the DSS metrics was to discern the superior tank design method and can be better evaluated using global metrics. The smaller the global metric value, the better indication of similarity. For the given instance, better similarity means superior performance. Applying the global metric, the calculated values are shown in
Table 13. For the exception of Tank Number Cases 6 and 7, the scaled design demonstrated lower metrics and surpassed the performance of the simple design. As the number of tanks was increased, the metric difference between the simple and scaled design also increased where the simple design was higher. This trend is comprehensible since the simple and scaled equation are a power different, as derived by Equation (48).

$$\text{simple: } \left(\frac{D_{reduced}}{D_{full}}\right) = \sqrt[3]{\frac{\dot{m}_{reduced}}{\dot{m}_{full}}}, \text{scaled: } \left(\frac{D_{reduced}}{D_{full}}\right) = \sqrt[4]{\frac{\dot{m}_{reduced}}{\dot{m}_{full}}} \tag{48}$$

As the mass flow rate is further reduced, the smaller the mass flow rate ratio becomes. Due to the power difference, the simple design will exaggerate the diameter reduction, especially when the mass flow rate is at smaller values. This is the main reason the simple design metric is growing faster than the scaled design. To explain why the scaled design metric suddenly increased for Tank Number Cases 6 and 7, further investigation into the simulation setup and datasets will be required.

Table 13. Measured global metric for simple and scaled multitank design in reference to the single-tank simulation results.

Tank No.	Simple Design Hot Tank Level Metric	Scaled Design Hot Tank Level Metric
2	2.506	2.432
3	3.603	3.159
4	4.906	3.742
5	6.750	4.636
6	8.367	31.432
7	11.416	29.881
8	16.094	10.941
9	28.512	8.980
10	30.638	8.327

5. CONCLUSIONS

The purpose of this report was to summarize the different possibilities regarding how scaling methodologies can assist in the realization of IES globally. Before any industry-scale NPP coupling with other power utilities or industrial process, regardless of whether the NPP is an ANPP or not, experimental and simulation base pilot-scale demonstrations are required to test the validity of the IES infrastructure. The report provided two possibilities: (1) data projection to run two or more facilities digitally in real-time; and (2) introducing the EMDAP approach to IES system design. For the data projection, an attempt to demonstrate and validate DETAIL scaling activities was made. In theory, if the projected data closely predicts the altered experiment or simulation, providing an adapter to convert the data from one scale to another can enable system to system interactions while preserving the dominant physics. The benefit of such a capability is massive considering the range of facility interaction is significantly broadened. The given demonstration case projecting an accelerated case of a thermal storage and hydrogen production IES provided a first look of possible issues, such as the normalization method selection being appropriate for the application case. For the EMDAP adaption to system design, a modified process of the EMDAP was developed and applied to an indirect two-tank heat storage system design. System phenomena were identified, ranked, and scaled to discover helpful key relations that would determine the ideal component geometry. In future INL IES program activities, the developed capabilities will be further refined as the research reported in this report are simple cases.

6. REFERENCES

1. Morton, T. J. 2020. “Integrated Energy Systems Experimental Systems Development.” U.S. Department of Energy. https://www.osti.gov/servlets/purl/1668842.
2. Levin, T., et al. 2022. “Extreme Weather and Electricity Markets: Key Lessons from the February 2021 Texas Crisis.” *Joule* 6(1): 1–7. https://doi.org/10.1016/j.joule.2021.12.015.
3. Eliana, R. 2022. “Argentina Capital Hit by Major Power Outage Amid Heat Wave.” News Article: Reuters. Accessed 31 May 2022. https://www.reuters.com/world/americas/argentina-capital-hit-by-major-power-outage-amid-heat-wave-2022-01-11/.
4. Ma, J., et al. 2022. “Carbon Capture and Storage: History and the Road Ahead.” *Engineering* 14: 33–43. https://doi.org/10.1016/j.eng.2021.11.024.

5. Bragg-Sitton, S. M. 2022. “Next Generation Nuclear Energy: Advanced Reactors and Integrated Energy Systems.” INL/MIS-22-66708, Idaho National Laboratory, Idaho Falls, Idaho. Accessed 31 May 2022. https://www.osti.gov/servlets/purl/1865609.
6. Frick, K. L., A. Alfonsi, C. Rabiti, and D. M. Mikkelson. 2021. “Hybrid User Manual.” INL/MIS-20-60624-Rev001; Idaho National Laboratory: Idaho Falls, ID, USA. Accessed 22 June 2023. https://www.osti.gov/biblio/1863262.
7. Brück, D. Dymola Referential. 12 April 2023. Accessed 22 June 2023. https://www.3ds.com/fileadmin/PRODUCTS/CATIA/DYMOLA/PDF/Dymola-referential-2023.pdf.
8. Reyes, J. N. 2015. “The Dynamical System Scaling Methodology.” In proceedings of the 16th International Topical Meeting on Nuclear Thermal Hydraulics, Chicago, IL.
9. Reyes, J. N.; C. Frepoli, and J. P. Yurko. 2015. “The Dynamical System Scaling Methodology: Comparing Dimensionless Governing Equations with the H2TS and FSA Methodologies.” In proceedings at the 16th International Topical Meeting on Nuclear Thermal Hydraulics, Chicago, IL
10. Reyes, J. N., and C. Frepoli. 2019. “Similarity and Scaling.” In *Design-Basis Accident Analysis Methods for Light-Water Nuclear Power Plants, 1st ed*, edited by Robert P Martin and Cesare Frepoli, Chapter 6: 181–263. World Scientific, Singapore.
11. Brown, G. 1939. “The Evolution of Physics from Early Concepts to Relativity and Quanta. By Albert Einstein and Leopold Infeld (Cambridge: At the University Press, 1938).” *Philosophy*, 14(54), 242. https://doi.org/10.1017/S0031819100011670.
12. Modelica Association. 2023. “Modelica – A Unified Object-Oriented Language for Systems Modeling Language Specification, Version 3.6.” Accessed 7 November 2023. https://specification.modelica.org/maint/3.6/MLS.pdf.
13. Yoshiura, R., S. Creasman, and A. Epiney. 2023. “Engineering-Scale Integrated Energy System Data Projection Demonstration via the Dynamic Energy Transport and Integration Laboratory.” *Energies* 16(16):5878. https://doi.org/10.3390/en16165878.
14. Frick, K., S. Bragg-Sitton, and C. Rabiti. 2020. “Modeling the Idaho National Laboratory Thermal Energy Distribution System (TEDS) in the Modelica Ecosystem.” *Energies* 13(23): 6353. https://doi.org/10.3390/en13236353.
15. Mikkelson, D. M., et al. 2022. “HYBRID Modeling of the DETAIL Experimental Facility.” INL/EXT-22-70396, Idaho National Laboratory, Idaho Falls, ID, USA. https://doi.org/10.2172/1985489.
16. Esence, T., et al. 2017. “A review on experience feedback and numerical modeling of packed-bed thermal energy storage systems.” *Solar Energy* 153: 628–654. https://doi.org/10.1016/j.solener.2017.03.032.
17. Frick, K. L., S. M. Bragg-Sitton, and C. Rabiti. 2020. “Development of the INL Thermal Energy Distribution System (TEDS) in the Modelica Eco-System for Validation and Verification.” INL/EXT-20-59195, Idaho National Laboratory, Idaho Falls, ID, USA, 2020. https://doi.org/10.2172/1668777.
18. Van Lew, J. T., et al. 2011. “Analysis of Heat Storage and Delivery of a Thermocline Tank Having Solid Filler Material.” *Journal of Solar Energy Engineering.* 133(2): 021003. https://doi.org/10.1115/1.4003685.
19. IEA. 2019. “Net Zero by 2050 Data Explorer.” 2021. Technical Report, International Energy Agency. https://www.iea.org/data-and-statistics/data-tools/net-zero-by-2050-data-explorer.
20. INL. 2010. “Nuclear-Integrated Methanol-to Gasoline Production Analysis.” Technical Report TEV-667. Idaho National Laboratory, Idaho Falls, ID.

https://art.inl.gov/NGNP/NEAC%202010/INL_NGNP%20References/TEV-667%20Nuclear-Integrated%20Methanol-to%20Gas.pdf.

21. Ramirez-Corredores, M.M., et al. 2021. “Identification of opportunities for integrating chemical processes for carbon (dioxide) utilization to nuclear power plants.”, *Renewable and Sustainable Energy Reviews*, 150: 111450. https://doi.org/10.1016/j.rser.2021.111450.
22. U.S. NRC. 2005. “Regulatory Guide 1.203: Transient and Accident Analysis Methods.” https://www.nrc.gov/docs/ML0535/ML053500170.pdf.
23. Yoshiura, R., A. Duenas, and A. Epiney. 2022. “Dynamical System Scaling of a Thermocline Thermal Storage System in the Thermal Energy Distribution System (TEDS) Facility.” *Energies* 15(12): 4265. https://doi.org/10.3390/en15124265.
24. Therminol Heat Transfer Fluids by Eastman. 2019. “Therminol 66 – heat transfer fluid.” Accessed 8 November 2023. https://www.therminol.com/sites/therminol/files/documents/TF-8695_Therminol-66_Technical_Bulletin.pdf.